ISSN: 3033-3652

Journal of Physical Mathematics & its Applications

SCIENTIFIC Research and Community

Review Article

Open Access

GLYBATOMAQ: A Proof-of-Concept Quantum-Geometric Rank-Audit Framework for GLIPR1 Screening Using Operator Kernels, DFT-Proxy/QMC-Style Proxy Refinement, and MQWalk Topology-Consistency Auditing

Ioannis Grigoriadis

Biogenetoligandorol, Department of Computer Drug Discovery Science (Biogenetor Stations), Thessaloniki, GLYBATOMAQ Stations, Thessaloniki, MQWalk™ R&D Units, Thessaloniki, Biogenea Pharmaceuticals Ltd, Thessaloniki, Greece

ABSTRACT

Background: Post-docking prioritization is vulnerable to near ties, protocol dependence, and overinterpretation of heterogeneous scores. Methods: We developed GLYBATOMAQ as a methodological proof-of-concept rank-audit framework for GLIPR1-focused virtual screening. A normalized positive-semidefinite operator construction defines ligand-pocket geometry; robust scaling harmonizes heterogeneous inputs; a DFT-proxy electronic-descriptor branch, a QMC-style proxy uncertainty branch, and MQWalk graph propagation contribute distinct, reliability-gated evidence to rank fusion. Results: In the HSX demonstration, HSX-cons2 remained first after reliability-aware fusion, whereas HSX-cons3 moved from rank 4 to rank 3 and HSX-cons4 moved from rank 3 to rank 4, demonstrating explicit near-tie auditing. The numerical demonstration uses transformed supplementary values and proxy or imputed branch inputs; no first-principles DFT calculation, QMC simulation, prospective experiment, or independent external benchmark was performed. Accordingly, the reported quantities characterize workflow behavior and rank movement rather than binding affinity or quantum-chemical energy. Conclusion: GLYBATOMAQ provides a formally specified and auditable decision architecture in which rank movement, proxy electronic support, uncertainty penalties, topology support, and diagnostic flags are explicit. Independent benchmark validation together with release of executable code and complete machine-readable data is required before predictive-performance or confirmatory claims.

***Corresponding author**

Ioannis Grigoriadis, Biogenetoligandorol, Department of Computer Drug Discovery Science (Biogenetor Stations), Thessaloniki, GLYBATOMAQ Stations, Thessaloniki, MQWalk™ R&D Units, Thessaloniki, Biogenea Pharmaceuticals Ltd, Thessaloniki, Greece.

Received: August 13, 2026; **Accepted:** August 17, 2026; **Published:** August 27, 2026

Keywords: GLIPR1, Quantum Geometry, Positive-Semidefinite Operator Kernels, Bures distance, Fubini-Study Metric, Quantum Fisher Information, DFT-Proxy/QMC-Style Proxy Refinement, MQWalk Topology-Consistency Audit, Rank Auditing, Virtual Screening

Introduction

Background and Motivation

Docking-centered virtual screening remains a practical tool for hypothesis generation when applied under fixed, reproducible protocols. Its main utility is comparative prioritization across large libraries rather than literal prediction of binding free energy. This distinction has long been emphasized in the docking literature. AutoDock Vina was introduced as an efficient docking framework for ranking under a defined scoring function [1]. AutoDock4 extended docking with selective receptor flexibility [2]. Glide provided a rapid docking and scoring scheme for pose assessment [3]. At the same time, Kitchen et al. noted that "significant challenges remain" in docking and scoring, and Warren et al. presented a critical benchmark-based assessment of docking programs and scoring functions [4,5]. Later reviews by Pagadala et al. and Guedes et al. likewise stressed that docking scores should be interpreted cautiously [6,7]. DockThor-VS extends this screening infrastructure, but it does not remove the underlying rank-centric character of the task [8]. Benchmark resources such as PDBbind, the docking sets of Huang et al., and DUD-E further reinforce that screening quality is judged primarily through ranking and enrichment behavior [9-11]. These limitations motivate the introduction of an explicit pattern-recognition layer capable of stabilizing representation, preserving comparability, and making rank behavior auditable. Such a layer is naturally grounded in kernel learning, support-vector methods, Gaussian-process reasoning, and positive-definite matrix analysis, with additional numerical support from approximation-theoretic and special-function tools [12-21]. The present study focuses on GLIPR1-oriented in silico screening and is anchored to experimentally determined human sGLIPR1 structures in the Protein Data Bank, specifically the structural study of Asojo et al. and the GLIPR1-related entries 3Q2U and 3Q2R [22-25]. Pocket definition is supported by Fpocket [26]. In this setting, the central problem is not only score generation, but also stable and interpretable ordering of candidates.

GLYBATOMAQ Concept and the Need for a Chemistry-Safe Consensus

GLYBATOMAQ addresses heterogeneous glioma-associated ligand collections through a hierarchical Hyper Mega Core (HMC) concept that is intentionally chemistry-safe. Rather than

enforcing atom-level fusion across non-comparable chemotypes, the framework defines consensus at the level of family-aware pharmacophore grammar and modular scaffold logic. This preserves medicinal-chemistry realism while enabling descriptor-space comparison and rank-based evaluation across diverse ligand families. This design is consistent with both classical and modern representational chemistry. Practical curation can be carried out with RDKit, Morgan-style structure encoding, extended-connectivity fingerprints, and SMILES-based normalization [27-30]. SELFIES provides a robust molecular string representation [31]. More structured generative and graph-based formulations, including grammar VAE, junction-tree VAE, graph-policy learning, recurrent molecular design, latent continuous molecular design, neural message passing, graph convolution, and attention-based architectures, all support the same broader principle: chemically meaningful comparison depends on structured validity and interpretable abstraction rather than indiscriminate atom-level merging [32-39]. Descriptor-space proximity, therefore, is not taken to imply synthetic mergeability. In GLYBATOMAQ, consensus representations are used for comparison, clustering, and ranking, not as synthetic templates.

GLYBATOMAQ as a Quantum-Enriched Ranking Extension

GLYBATOMAQ extends the base GLYBATOMAQ framework through a late-stage, quantum-enriched refinement layer positioned after docking-oriented pattern recognition and before final prioritization. The extension is deliberately conservative. Docking remains the fixed-protocol oracle, while pattern recognition remains the principal ranking machinery [1-3,8,12-15]. The added DFT-proxy, QMC-style proxy, and MQWalk components are used for re-ranking, uncertainty quantification, and topology-consistency audit rather than for efficacy or clinical inference. The term "quantum-enriched" is methodological, not physical. It denotes a refinement layer that supplements an existing rank frontier with deterministic electronic-structure cues, stochastic uncertainty-aware auditing, and graph-propagation-based topology checks. The DFT component is grounded in the Hohenberg–Kohn and Kohn–Sham framework, with standard interpretive support from Parr and Yang and Martin et al. [41-44]. The QMC component follows the uncertainty-aware logic of Foulkes et al. and Needs et al. [45,46]. MQWalk uses notation consistent with quantum-information formalisms, but its interpretation remains strictly algorithmic in view of broader cautions concerning extrapolation of quantum language to biology [47-49]. The workflow is therefore best understood as a rank augmentation scheme: Dock/Rank → Shortlist → DFT-proxy/QMC-style proxy/MQWalk → Fuse → Re-rank + Audit. This interpretation is also relevant to Pattern Recognition. Recent work has emphasized ranking-based learning, local-kernel graph learning, informative graph selection, dynamic graph representation, adaptive graph propagation, and molecular graph contrastive learning [50-55]. GLYBATOMAQ adopts the same broad principle in a molecular screening setting: reliable decisions on structured data require stable representation, explicit propagation logic, and interpretable uncertainty control.

Core Technical Contributions

GLYBATOMAQ defines three complementary proxy-based refinement components. First, the DFT-proxy branch uses compact electronic-descriptor surrogates for shortlisted candidates, including normalized energy-like terms, frontier-gap proxies, charge or dipole summaries, and reliability indicators. Its role is to exercise controlled separation of crowded near-tie regions without implying that first-principles electronic-structure calculations were completed. Second, the QMC-style proxy branch is restricted to a smaller candidate subset and represents uncertainty-aware energetic auditing through transformed energy-like estimates, dispersion penalties, interval-width surrogates, and sampling-quality indicators. These quantities demonstrate the intended uncertainty logic but are not outputs of variational or diffusion Monte Carlo simulations. Third, Avogadro-conditioned MQWalk topology-consistency auditing reuses the normalized operator-overlap graph to test whether proxy-supported promotions remain compatible with the topology implied by the representation layer. Its operator-kernel basis is grounded in kernel methods, positive-definite matrix structure, and bounded analytic conditioning, whereas the walk notation is borrowed from formal propagation language [12,15-21,40]. MQWalk is strictly algorithmic and does not imply biomolecular quantum transport [48,49].

Methods and Materials

GLYBATOMAQ Quantum-Enriched Re-Ranking Layer: DFT-Proxy/QMC-Style Proxy Auditing with MQWalk Topology Consistency

Scope, Rationale, and Methodological Placement within a Rank-Centric GLYBATOMAQ Workflow

GLYBATOMAQ is formulated as a late-stage, rank-centric mathematical-chemistry re-ranking layer rather than as a de novo docking, binding-free-energy, or generative-design engine. Its methodological purpose is deliberately narrow: to improve the interpretability and reliability of a pre-existing molecular ranking frontier by combining deterministic electronic descriptors, stochastic energetic uncertainty, and operator-kernel topology diagnostics. This placement is important because the proposed contribution is not the invention of a new docking score. Instead, GLYBATOMAQ addresses a recurring mathematical-chemistry problem: how to decide whether a ligand promoted by a screening pipeline is supported simultaneously by local electronic structure, uncertainty-aware energetic evidence, and global similarity topology.

Docking is therefore treated as a fixed-protocol comparative signal, not as an experimental surrogate. AutoDock Vina, AutoDock4, Glide, and DockThor-VS are used only to define an upstream ranking frontier. This interpretation follows established cautions in the docking literature [1-3,8]. Kitchen et al. noted that "significant challenges remain" in docking and scoring, Warren et al. critically assessed scoring-function behavior, and subsequent reviews likewise emphasized docking as a comparative prioritization tool rather than a literal affinity estimator [4-7]. Benchmark context is further provided by PDBbind, the docking test sets of Huang et al., and DUD-E [9-11]. Thus, the first methodological safeguard is conceptual: docking creates a hypothesis-generating frontier, whereas GLYBATOMAQ audits rank movement within that frontier.

The structural context is introduced through the Protein Data Bank, the GLIPR1 structural study of Asojo et al., and the GLIPR1-related structures 3Q2U and 3Q2R, with pocket localization supported by Fpocket [22-26]. These structures define the protein-side objects on which the downstream rank audit operates. Importantly, the protein pockets are not treated as interchangeable docking boxes. They are treated as distinct local chemical environments, each inducing its own ligand ordering, operator representation, and refinement uncertainty. This pocket-conditioned design is essential because mathematical-chemistry rank stability is rarely global: a ligand may be plausible in one structural microenvironment and weakly supported in another.

The re-ranking layer is invoked only for a pre-ranked shortlist and resolves near ties through three coupled branches: a DFT-

proxy branch for deterministic electronic-descriptor surrogates, a QMC-style proxy branch for uncertainty-aware energetic stress testing, and MQWalk for topology-consistency auditing against the upstream positive-semidefinite operator-kernel similarity space [12,15,41-47] . The coupling is constrained by evidence class. The DFT-proxy branch contributes local descriptor structure; the QMC-style proxy branch contributes uncertainty penalties; and MQWalk tests whether a rank promotion remains compatible with the ligand-pocket similarity geometry that placed the candidate in the shortlist. The resulting output is a decomposable rank-audit event rather than a claim that first-principles refinement was performed.

The term "quantum walk" is used strictly as an algorithmic graph-propagation analogy and not as a claim that biomolecular recognition is mediated by coherent quantum transport. This distinction is explicit to avoid overinterpretation and is consistent with the cautions of Arndt et al. and Nunn et al. [48,49]. In GLYBATOMAQ, MQWalk is a controlled mathematical diagnostic on a normalized operator graph. It is used to ask whether rank promotions remain stable under unitary-style propagation on the similarity network, not to claim a physical quantum walk inside GLIPR1.

Evidence classification. "Computed" is reserved for a calculation executed under a fully specified electronic-structure or Monte Carlo protocol with raw outputs and convergence diagnostics. "Proxy" denotes a transformed, normalized, supplementary, or imputed value used to exercise the audit logic. All numerical values assigned to the DFT-proxy and QMC-style proxy branches in the present Results are proxy quantities unless an explicit calculation record is supplied. The analysis therefore constitutes a methodological proof-of-concept rather than first-principles validation.

Operationally, the Workflow is:
Supporting visual evidence is supplied in SI Appendix I and is cited individually throughout the analysis. SI Appendix I, Figure 1 presents the quantum-enriched refinement circuit, topology/transport diagnostics, and the MMP3 ranking/affinity benchmark context. SI Appendix I, Figure 2 presents the rank-centric circuit with vortioxetine glioblastoma network-pharmacology and docking numerics. SI Appendix I, Figure 3 presents the HSX-cons1–4 Mega-Core dashboard and reporting plots. SI Appendix I, Figure 4 presents the biology-facing MBHA optimization, interaction-persistence, stability-filtering, and QSAR panel. SI Appendix I, Figure 5 presents the DFT-proxy diagnostics, fusion logic, and comparative docking-energy overview. SI Appendix I, Figure 6 integrates hotspot landscapes, MQWalk topology-consistency audit, and residue-resolved energetic fingerprints. SI Appendix I, Figure 7 presents the rank-first Vina leaderboard with refinement and hotspot context. SI Appendix I, Figure 8 presents the comparative AutoDock Vina ranking, pocket-resolved matrix, top-10 leaderboard, and audit trail. SI Appendix I, Figure 9 presents the DockThor 3Q2R affinity and energy-component results. These supplementary panels provide context for main Figures 1–5 and Tables 12–15.

Dock/Rank → Shortlist → DFT-proxy/QMC-style proxy/MQWalk → Fuse → Re-rank + Audit as illustrated in SI Appendix I, Figure 1A and SI Appendix I, Figure 2. The returned object is not a single scalar score but a rank-audit bundle containing the base score Sθ, DFT-proxy support S_DFT-proxy, QMC-style proxy support S_QMC-style, MQWalk support S_MQW, branch-reliability terms, diagnostic penalties, and the post-refinement rank shift ΔR. This distinction is central to the mathematical-chemistry value of the method: the output is a structured explanation of ranking evidence rather than a black-box replacement score. The formulation is naturally aligned with Pattern Recognition because the primary object is a structured ranking problem, consistent with ranking-based transformation, local-kernel graph learning, informative graph selection, dynamic graph representation, adaptive graph propagation, and molecular graph contrastive learning [50-54].

Inputs, Data Model, and Candidate-Selection Boundary
The GLYBATOMAQ refinement layer consumes only protocol-logged upstream outputs. These include pocket definitions anchored to 3Q2U and 3Q2R, optionally cross-checked by Fpocket; a ligand set curated under chemistry-safe provenance; docking outputs generated under fixed settings; and the base GLYBATOMAQ score Sθ, which defines the pre-refinement frontier while remaining distinct from docking [24-26]. This separation prevents circular interpretation: docking contributes poses and an initial comparative frontier, whereas Sθ defines the model-derived order to be audited.

The chemistry-safe representation layer is compatible with MMFF94 geometry handling, RDKit, Morgan-style encodings, ECFP fingerprints, SMILES, and SELFIES [27-32]. It is also compatible with structured molecular learning approaches including grammar VAE, junction-tree VAE, graph-policy learning, recurrent molecular design, latent continuous design, neural message passing, graph convolution, and attention-based architectures [32-39]. These representations are not introduced as independent claims of predictive superiority. Rather, they define admissible molecular encodings from which stable candidate objects and operator summaries can be constructed.

At the operator level, pocket and ligand topology inputs are summarized by positive-semidefinite matrices ρ_P and ρ_L. A typical construction is

$$\rho\_X = n\_X^{-1} X X^T, \rho\_X \succeq 0, X \in \{P,L\} \quad (1)$$

where X is a logged feature or embedding matrix after preprocessing, n_X is the number of encoded objects or local descriptors, and ρ_X is therefore a Gram-type positive-semidefinite operator. The ligand–pocket similarity is then expressed through the normalized overlap kernel

$$\bar{K}(P,L) = Tr(\rho\_P \rho\_L) / \sqrt{([Tr(\rho\_P^2)Tr(\rho\_L^2)] + \varepsilon)} \quad (2)$$

This quantity has two roles. First, it provides a scale-controlled similarity measure between protein-pocket and ligand operator summaries. Second, it supplies the graph weights used by MQWalk validation. Because $\bar{K}(P,L)$ is derived from positive-semidefinite objects, the resulting geometry is compatible with kernel learning, Gaussian-process similarity concepts, and positive-definite matrix theory [12,14,15]. This operator-overlap construction replaces an isolated ligand score with a trace-normalized comparison between pocket and ligand chemical-information operators.

The role of this stabilizing layer between docking and refinement is shown in SI Appendix I, Figure 2 and recurs in SI Appendix I, Figure 6. In practical terms, a ligand can be promoted after DFT-proxy/QMC-style proxy refinement only if the promotion is not discordant with the underlying operator-kernel topology. This prevents the refinement layer from acting as an unconstrained score amplifier.

To control computational cost and to preserve the intended statistical meaning of the procedure, refinement is applied only to shortlist candidates defined by

$$\mathcal{L}\_top(P) = \{L \in \mathcal{L}\_P : rank[S\_\theta(P,L)] \leq K\_short\} \quad (3)$$

When required, a consensus shortlist is pooled across pockets. Each evaluated pairis stored as a candidate object

$$\mathcal{O}(P,L) = (P,L,\chi\_L,D(P,L),S\_\theta(P,L),\rho\_P,\rho\_L,\bar{K}(P,L),\Pi\_prov) \quad (4)$$

where χ_L denotes the conformer ensemble and Π_prov records provenance, descriptor settings, conformer source, docking protocol, and refinement status. The purpose of this object is traceability. Any rank movement must be traceable to a defined input, descriptor, uncertainty estimate, or topology diagnostic. The shortlist-and-branch logic is illustrated in SI Appendix I, Figure 1A, while the chemistry-safe HSX anchor view is visible in SI Appendix I, Figures 2 and 3.

Shared Conditioning, Robust Scaling, and Avogadro-Anchored Numerical Regularization

Before branch scoring, all candidate features are subjected to shared conditioning. For each feature channel x_j, a robust standardized value is computed as

$$z\_j = [x\_j - median(x\_j)] / [MAD(x\_j) + \varepsilon] \quad (5)$$

This choice is used because shortlist distributions are typically small, heavy-tailed, and sensitive to outliers. A mean–variance normalization would allow a single unstable electronic or docking-derived channel to dominate the branch fusion. Robust normalization therefore serves a mathematical role: it converts heterogeneous chemical descriptors into bounded, comparable evidence components.

The standardized channel is then scaled by an Avogadro-anchored numerical factor

$$a\_N = \exp(-\alpha \ln N\_A) = N\_A^{(-\alpha)} \quad (6)$$

and bounded as

$$\hat{x}\_j = \tanh(a\_N z\_j) \quad (7)$$

where the CODATA Avogadro constant is used only as a deterministic scale anchor [43]. This step is numerical rather than physical, and no molecular-counting interpretation is assigned to the scaling factor. The anchor defines a deterministically specified, dimension-aware damping convention for combining graph, electronic-proxy, and uncertainty-support quantities while limiting domination by channels with larger native scales.

Shared conditioning is applied before branch fusion, as illustrated in SI Appendix I, Figure 2 and SI Appendix I, Figure 5B. Robust standardization and bounded transformation constrain the influence of heterogeneous channels and make the branch inputs explicitly traceable for audit before they are allowed to affect rank movement.

DFT-Proxy Branch: Internal Descriptor Demonstration for Near-tie Separation

The DFT-proxy branch is conceptually motivated by the Hohenberg–Kohn and Kohn–Sham formalism and by standard DFT treatments [41,44]. No electronic-structure calculation was executed for the numerical demonstration. All values reported for this branch are normalized internal descriptor proxies derived from supplementary score axes; they are not Kohn–Sham energies, orbitals, densities, convergence outputs, or first-principles protein–ligand energetics. Equations (8)–(12) formalize the branch scoring structure; in the present proof-of-concept, the structure is evaluated with proxy descriptors rather than first-principles outputs.

For a logged candidate geometry, the formal descriptor basis is the Kohn–Sham relation

$$[-\tfrac{1}{2}\nabla^2 + v\_eff[\rho](r)]\psi\_i(r) = \varepsilon\_i\psi\_i(r) \quad (8)$$

together with the variational condition

$$\delta E\_KS[\rho]/\delta\rho(r) = \mu \quad (9)$$

For a future calculation, the branch would extract a descriptor vector

$$\Phi\_DFT\text{-}proxy = (E\_proxy,\Delta\varepsilon\_HL,\mu\_e,\eta\_e,\omega\_e,q\_res,\mu\_dip,c\_SCF) \quad (10)$$

where the specific components are selected from logged electronic descriptors, frontier-orbital summaries, charge descriptors, local contact descriptors, and density-derived quantities. The exact descriptor list is fixed before evaluation to avoid post hoc selection.

The DFT-proxy branch score is written as

$$S\_DFT\text{-}proxy(P,L) = \beta\_D^{T}\Phi\_DFT\text{-}proxy(P,L) \quad (11)$$

with a reliability gate

$$r\_DFT\text{-}proxy = I\_SCF\ I\_geom\ I\_domain\ I\_complete \quad (12)$$

The reliability term records convergence quality, geometry stability, descriptor completeness, and whether the electronic-descriptor proxies fall within the calibration envelope of the shortlist. Thus, the DFT-proxy contribution is retained only when the corresponding proxy record satisfies the predefined reliability criteria. If the descriptor inputs are incomplete, unstable, or outside the expected numerical domain, the DFT-proxy contribution is down-weighted rather than silently retained.

This branch is visualized most directly in the descriptor histograms and scatter diagnostics of SI Appendix I, Figure 5A. Its mathematical-chemistry contribution is a controlled, reliability-gated electronic-descriptor perturbation of the rank frontier. It is not interpreted as a first-principles DFT scoring replacement.

QMC-Style Proxy Branch: Internal Uncertainty Demonstration

The QMC-style proxy branch is conceptually motivated by uncertainty-aware stochastic energetic analysis [48,49]. No variational or diffusion quantum Monte Carlo simulation was executed for the numerical demonstration. All values reported for this branch are internal uncertainty-support proxies constructed from supplementary or transformed inputs; they are not sampled local energies, Monte Carlo variances, confidence intervals, effective sample sizes, or first-principles QMC results. Equations (13)–(17) formalize the intended uncertainty-aware branch structure and are used here only as a proxy-scoring specification.

For each audited pocket–ligand pair (P,L), the QMC-style proxy branch defines an estimated energy-like quantity

$$\bar{E}\_QMC\text{-}style = M^{-1} \Sigma\_(m=1)^M E\_L(R\_m) \quad (13)$$

an uncertainty estimate

$$\sigma\_QMC\text{-}style^2 = (M-1)^{-1} \Sigma\_(m=1)^M [E\_L(R\_m)-\bar{E}\_QMC\text{-}style]^2 \quad (14)$$

and a confidence-width summary

$$CI\_QMC\text{-}style = z\_(1-\alpha/2)\ \sigma\_QMC\text{-}style / \sqrt{M\_eff} \quad (15)$$

The conservative QMC-style proxy score is defined as

$$S\_QMC\text{-}style = -\bar{E}\_QMC\text{-}style - \lambda\_\sigma\ \sigma\_QMC\text{-}style - \lambda\_CI\ CI\_QMC\text{-}style \quad (16)$$

This expression penalizes uncertain energy-like estimates. A candidate is not promoted solely by a favorable proxy expectation when that expectation is accompanied by a broad uncertainty surrogate. The QMC-style proxy branch therefore requires rank promotion to survive both the expected support term and the uncertainty attached to that term.

The QMC-style proxy contribution is gated by

$$r\_QMC\text{-}style = I\_sample\ I\_var\ I\_CI\ I\_conv \quad (17)$$

The reliability gate records sampling adequacy, variance behavior, confidence-width stability, and convergence-related diagnostics in the formal branch definition. Within the present proof-of-concept, inflated uncertainty-support proxies are flagged rather than silently retained because they can indicate conformational ambiguity, local-geometry sensitivity, or instability of the energy-like surrogate. The QMC-style proxy branch is summarized in SI Appendix I, Figures 2 and 3 and enters the fusion shown in SI Appendix I, Figure 5B.

MQWalk Branch: Operator-Kernel Topology-Consistency Audit of Rank Promotions

MQWalk is the topology-validation branch of GLYBATOMAQ. Its purpose is to determine whether proxy-supported rank movement remains consistent with the ligand–pocket similarity geometry induced by the normalized operator-overlap kernel. Unlike DFT-proxy and QMC-style proxy, MQWalk does not add a physical electronic-energy model. It is a mathematical diagnostic on the shortlist graph.

Starting from the normalized overlap kernel $\bar{K}(P,L)$, a bipartite pocket–ligand adjacency matrix is defined as

$$A\_PL(P,L) = \bar{K}(P,L) \quad (18)$$

The degree-normalized adjacency is

$$A\_N = D^{(-1/2)}\ A\ D^{(-1/2)} \quad (19)$$

where D is the diagonal degree matrix. To prevent disconnected or weakly connected shortlist components from producing unstable propagation behavior, teleport mixing is introduced:

$$A\_\gamma = (1-\gamma)A\_N + \gamma 11^T/|V| \quad (20)$$

The Avogadro-conditioned graph Laplacian is then

$$\tilde{L} = N\_A^{(-\alpha)}(I-A\_\gamma) \quad (21)$$

Propagation is written as

$$U(t) = \exp(-it\tilde{L}) \quad (22)$$

and the node mass at node j is

$$p\_j(t) = |\langle j|U(t)|\psi_0\rangle|^2 \quad (23)$$

These quantities are interpreted only as topology-consistency diagnostics. The central question is whether a promoted ligand remains close, under graph propagation, to the pocket and ligand neighborhoods that justified its initial ranking. If a candidate receives strong DFT-proxy or QMC-style proxy support but is topologically isolated from chemically similar pocket–ligand neighborhoods, the promotion is marked as discordant.

The MQWalk score is defined as

$$S\_MQW = \lambda\_walk\langle p(t)\rangle\_path - \lambda\_disc\Delta\_top \quad (24)$$

Here, $\langle p(t)\rangle\_path$ summarizes propagation-supported proximity, while Δ_topo penalizes discordance between branch-level promotion and graph-level neighborhood consistency. In practice, MQWalk functions as a graph-consistency filter rather than as an additional physical model. It is specifically designed to prevent unsupported rank jumps caused by a single favorable branch score.

This branch is represented in SI Appendix I, Figure 1B–C, SI Appendix I, Figure 3, and SI Appendix I, Figure 6. Its main mathematical-chemistry innovation is that ligand prioritization is constrained not only by scalar descriptors but also by the topology of a positive-semidefinite ligand–pocket operator space.

Rank Movement, Diagnostic Penalties, and Reliability-Aware Fusion

Rank movement is audited explicitly. For each pocket–ligand pair, the pre-refinement rank is $R_0(P,L)$, the post-refinement rank is $R^+(P,L)$, and the rank shift is

$$\Delta R(P,L) = R_0(P,L) - R^+(P,L) \quad (25)$$

A positive ΔR indicates promotion, while a negative ΔR indicates demotion. Rank stability is summarized by

$$Overlap@k = |Top\_k(R_0) \cap Top\_k(R^+)|/k \quad (26)$$

Rank stability is included because a refinement layer should not arbitrarily destroy the upstream frontier. A low Overlap@k value is not automatically erroneous, but it requires support from DFT-proxy evidence, QMC-style proxy evidence, or topology-supported correction. Rank movement is therefore treated as an auditable outcome that requires an explicit evidence trail.

Diagnostic penalties are collected in

$$\Pi\_diag = \lambda\_D(1-r\_DFT\text{-}proxy) + \lambda\_Q(1-r\_QMC\text{-}style) + \lambda\_T\Delta\_topo + \lambda\_MI\_missing \quad (27)$$

which includes flags for low DFT-proxy reliability, inflated QMC-style proxy uncertainty, convergence failure, descriptor-domain violation, topology discordance, or missing provenance. These

flags determine whether a candidate's final rank is classified as supported, weakly supported, or audit-failed.

The final fused score is

$$S^{+}(P,L) = w_0 S\_\theta + w\_Dr\_DFT\text{-}proxy S\_DFT\text{-}proxy + w\_Qr\_QMC\text{-}style S\_QMC\text{-}style + w\_MS\_MQW - \Pi\_diag \quad (28)$$

All weights are predeclared or logged for traceability. The fusion rule is therefore not an opaque ensemble. It is a reliability-aware evidence-integration rule in which each branch has a distinct mathematical role:

- preserves the upstream ranking frontier.
- introduces deterministic electronic-structure separation.
- introduces uncertainty-penalized energetic auditing.
- constrains rank movement by operator-kernel topology.
- prevents unreliable branch evidence from being overinterpreted.

The full fused logic is summarized in SI Appendix I, Figure 5B, while SI Appendix I, Figure 6 links hotspot, topology, and residue-level evidence within a common audit trail. The audit-first construction constrains model complexity by assigning each component a nonredundant role in the rank-audit chain; a branch is informative only to the extent that it contributes distinct, traceable evidence.

Pocket-Specific and Consensus Leaderboards

Because pocket-dependent reversals are expected, the method reports both pocket-specific leaderboards and a consensus leaderboard. For each pocket P, the pocket-specific leaderboard is obtained by sorting the fused score $S^{+}(P,L)$. This preserves the possibility that different GLIPR1 pocket environments support different ligand hypotheses.

The consensus score is defined as

$$S\_cons(L) = Agg\_(P\in\mathcal{P})\{S^{+}(P,L)\} \quad (29)$$

where the aggregation rule is predeclared and logged. The aggregation may be a mean, trimmed mean, rank-product, Borda-type statistic, or another fixed rank-aggregation rule, but it is specified before final leaderboard evaluation. The consensus result is therefore a pre-specified summary of pocket-conditioned evidence rather than a post hoc selection of the most favorable pocket result.

This reporting strategy is consistent with benchmark-aware docking practice discussed by Kitchen et al. Warren et al. Pagadala et al. Guedes et al. Huang et al. and Mysinger et al. and with recent Pattern Recognition work emphasizing ranking, graph consistency, and structured aggregation rather than isolated scalar decisions [4-7,10,11,50-55]. In practical terms, the pocket-wise and consensus views implement the audit-first logic: docking defines the initial frontier, refinement resolves near ties, topology checks constrain unsupported jumps, uncertainty terms penalize unstable energetic evidence, and the final output is a protocol-specified, auditable leaderboard rather than an opaque score list. This interpretation is reinforced across SI Appendix I, Figures 1, 2, 5, 6, and 7–9.

Quantum-Geometric 2D Formalization of MQWalk-MBHA-Guided Pharmacophore Assembly Scope of the Quantum-Geometric Construction

GLYBATOMAQ expresses the two-dimensional HMC assembly process as a quantum-geometric optimization problem on a constrained pharmacophore manifold. The construction is mathematical and algorithmic. It does not assert coherent quantum transport in GLIPR1, atom-exact fusion of all modules, a synthetic route, binding affinity, biological efficacy, or therapeutic activity. Instead, it yields a formal certificate in which ordered pharmacophore paths are jointly constrained by planar geometry, operator compatibility, graph topology, curvature regularity, and uncertainty-aware rank evidence [12,15,32,33,37,38,41-49].

HMC Role Grammar as a Constrained 2D Pharmacophore Manifold

Let the Hyper Mega Core grammar be represented by six ordered pharmacophore-role classes. The first five roles define the mandatory assembly backbone, whereas the sixth role represents an optional terminal cap or tail used only when the candidate design requires it:

$$\mathcal{G}\_HMC = (\boldsymbol{\mathcal{M}}_1,\boldsymbol{\mathcal{M}}_2,\boldsymbol{\mathcal{M}}_3,\boldsymbol{\mathcal{M}}_4,\boldsymbol{\mathcal{M}}_5,\boldsymbol{\mathcal{M}}_6) \quad (30)$$

The roles correspond to recognition nucleus, linker, interaction node, spacer, polarity/solubility module, and optional tail/cap. An admissible GLYBATOMAQ-HSX candidate is therefore an ordered typed chain rather than an arbitrary mixture of fragments:

$$L = (m_1,m_2,m_3,m_4,m_5,m_6), m\_i \in \boldsymbol{\mathcal{M}}\_i \quad (31)$$

Each module is embedded in a planar pharmacophore chart by an anchor coordinate, an orientation, and a compact footprint. Thus the local 2D state of module i is

$$q\_i = (p\_i,\varphi\_i,G\_i), p\_i=(x\_i,y\_i)\in\mathbb{R}^2,\varphi\_i\in S^1 \quad (32)$$

The complete planar assembly is the ordered object

$$L\_2D = \{q\_i\}\_(i=1)\text{^}6, e\_i=[p\_i,p\_(i+1)], i=1,\ldots,5 \quad (33)$$

The feasible pharmacophore manifold is defined by role order, edge-length bounds, angular bounds, orientation compatibility, and non-overlap of non-adjacent footprints:

$$\boldsymbol{\mathcal{F}}\_2D = \{L\_2D : d\_(i,min)\le\|p\_(i+1)-p\_i\|\le d\_(i,max),\ \theta\_(i,min)\le\theta\_i\le\theta\_(i,max),\ |\varphi\_(i+1)-\varphi\_i|\le\eta\_i\} \quad (34)$$

This manifold excludes disconnected, collapsed, and topologically incoherent arrangements while preserving the chemistry-safe interpretation of the HMC. The role grammar specifies which pharmacophore functions may be adjacent; the 2D feasibility constraints specify how those functions may be geometrically realized.

Operator-Valued Anchors and Normalized Quantum-Geometric Overlap

To couple the planar pharmacophore chain to the operator-kernel layer, each module is assigned a local feature matrix Z_i and a positive-semidefinite operator. This construction parallels the pocket-ligand PSD representation used throughout the GLYBATOMAQ ranking layer:

$$\rho\_i = Z\_i^{T}Z\_i/Tr(Z\_i^{T}Z\_i), \rho\_i\ge 0, Tr(\rho\_i)=1 \quad (35)$$

The module operator is therefore a normalized density-like descriptor object. It is not interpreted as a physical molecular density matrix; it is an auditable quantum-geometric representation of local pharmacophore information. Compatibility between adjacent modules is measured by normalized trace overlap,

$$\bar{K}_{ij} = \mathrm{Tr}(\rho_i \rho_j)/\{\sqrt{[\mathrm{Tr}(\rho_i^2)\mathrm{Tr}(\rho_j^2)]} + \varepsilon\} \quad (36)$$

A role-adjacent edge is admitted only when descriptor-space overlap and geometric feasibility are satisfied simultaneously:

$$(m_i, m_{(i+1)}) \in E \Leftrightarrow [\bar{K}_{(i,i+1)} \geq \tau_i] \wedge [L_{2D} \in \mathcal{F}_{2D}] \quad (37)$$

The connection step is therefore a kernel-permission rule rather than a freehand scaffold-merge operation. It couples local 2D pharmacophore geometry to a PSD operator overlap, so that each edge has both geometric and descriptor-space justification [12,15].

Reliability-Weighted Quantum-Geometric Objective and Formal Characterization

The DFT-proxy and QMC-style proxy branches refine the generated path by attaching deterministic electronic descriptors and uncertainty-aware energetic evidence to an already admissible HMC assembly [41-46]. The enriched final objective is

$$S_{QG^+}(P,L) = w_0 S_\theta + w_{Dr} D_S D + w_{Qr} Q_S Q + w_{MS} M + w_{path} S_{path} - \Pi_{diag} - \Pi_{curv} - \Pi_{QG} \quad (38)$$

Here Π_{QG} collects distance, metric, and projection-residual penalties not already represented in Π_{diag} or Π_{curv}. The final GLYBATOMAQ-HSX candidate is obtained by

$$L^* = \arg\max_{L \in \mathcal{F}_{2D} \cap \mathrm{Path}(H) \cap \mathrm{QG}(H)} S_{QG^+}(P,L) \quad (39)$$

Proposition (formal characterization). Under the HMC grammar, PSD operator mapping, quantum-geometric metric, Bures-distance edge rule, curvature-consistency penalty, MQWalk topology support, MBHA projection, and reliability-weighted DFT-proxy/QMC-style proxy fusion, GLYBATOMAQ-HSX ligand generation is a constrained quantum-geometric graph optimization problem rather than an arbitrary scaffold-fusion procedure.

Derivation. The HMC grammar fixes the pharmacophore roles and their order. The planar feasibility set fixes the allowable 2D anchor, angle, orientation, and non-overlap geometry. PSD operator mapping assigns each module a normalized descriptor operator, and trace overlap plus Bures-style distance determines which role-adjacent pairs may be connected. The metric g_{ab}, geodesic energy, and curvature penalty constrain abrupt descriptor-space deformation and path-dependent inconsistency. MQWalk then tests whether the assembled path is supported by the operator-overlap graph. MBHA proposes new candidates only through projection into the feasible quantum-geometric domain. Finally, DFT-proxy, QMC-style proxy, MQWalk, diagnostic, curvature, and projection terms are combined in the reliability-weighted score. By construction, any accepted candidate has an explicit assembly certificate:

$$\mathrm{Certificate}(L) = \{\text{role order}, \mathcal{F}_{2D}, \text{PSD overlap}, D_B \text{ bound}, \text{curvature consistency}, \text{MQWalk support}, \text{MBHA projection}, \text{proxy audit}\} \quad (40)$$

This certificate records that GLYBATOMAQ-HSX outputs are formally specified 2D quantum-geometric pharmacophore hypotheses for GLIPR1-oriented ranking. They remain computational design hypotheses and should not be interpreted as experimentally validated ligands, therapeutic structures, or synthetic prescriptions.

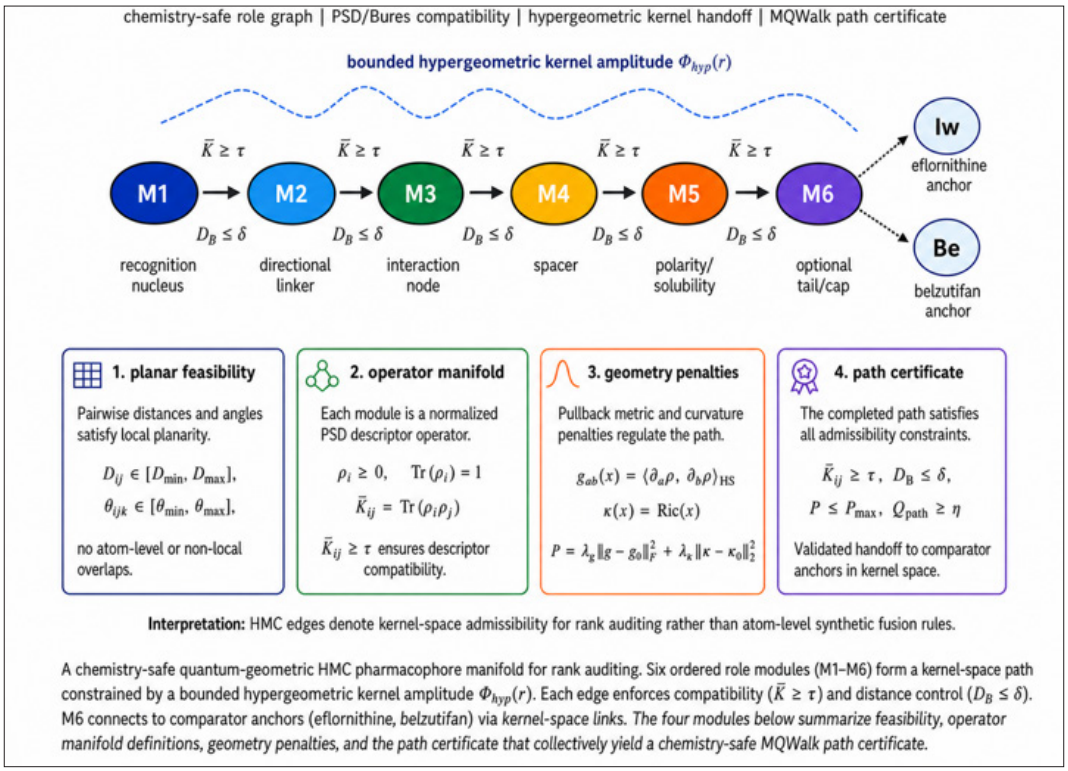

Figure 1: Quantum-Geometric HMC Pharmacophore Manifold and Chemistry-Safe Assembly Certificate. The HMC is Shown as an Ordered Pharmacophore-Role Manifold Rather than an Atom-Exact Fused Scaffold. Modules are Admitted only when Planar Feasibility, Normalized PSD Operator Overlap, Bounded Hypergeometric Kernel Compatibility, Bures/Fubini-Study Distance Control, Curvature Smoothness, MQWalk Path Support, and DFT-Proxy/QMC-Style Proxy Reliability are Simultaneously Compatible. Comparator Anchors are Linked only in kernel Space, Preserving Chemistry-Safe Interpretation

Quantum-Geometry Reporting Module and Diagnostic Interpretation

The framework includes a reporting module that separates quantum-geometric definitions from numerical proxy claims. Each metric, distance, curvature, sensitivity, and topology term is linked to a specific decision in the GLYBATOMAQ rank-audit workflow, making the mathematical contribution inspectable at candidate level.

The central object is a normalized PSD descriptor operator, rho(x), attached to a ligand, pocket, residue-contact neighborhood, or HMC role module. Local perturbations in x define a pullback metric g_ab(x), pairwise comparisons define overlap and Bures-style distances, path continuity is controlled by geodesic energy and curvature penalties, and MQWalk evaluates whether the resulting candidate path retains support in the operator-overlap graph. These quantities are interpreted as computational geometry diagnostics, not as direct physical observables.

Figures 1–5 and Tables 12–15 summarize the quantum-geometric reporting architecture. Figure 1 defines the chemistry-safe HMC manifold and assembly certificate; Figure 2 links bounded hypergeometric operator amplitudes to the DFT-proxy/QMC-style proxy/MQWalk audit circuit; Figure 3 presents the proxy-overlay generalization surface; Figure 4 provides the normalized quantum-geometry reporting matrix; and Figure 5 presents the MQWalk topology-consistency graph.

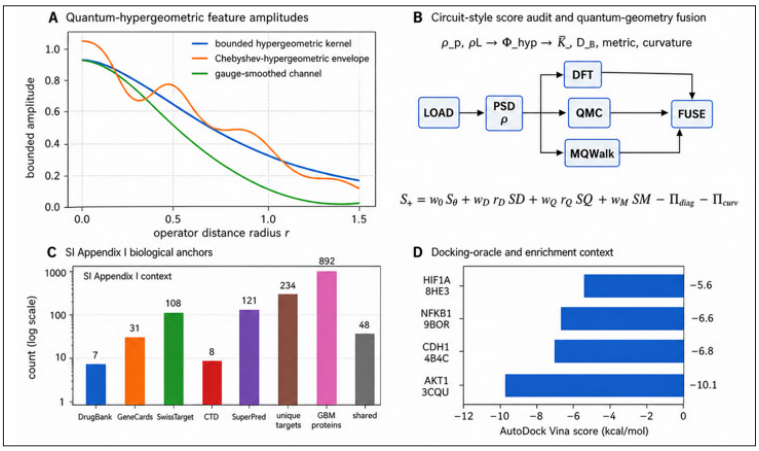

Figure 2: Quantum-Hypergeometric Dft-Proxy/QMC-Style Proxy/MQWalk Audit Circuit. Bounded Hypergeometric and Chebyshev-Hypergeometric Feature Channels Define Operator Amplitudes that are Passed Through PSD Encoding, DFT-Proxy Descriptor Scoring, QMC-Style Proxy Uncertainty-Aware Refinement, MQWalk Topology-Consistency Audit, and Reliability-Weighted Fusion. Biological Anchors from SI Appendix I, Figure 2 are Included as Target-Harvesting and Docking-Oracle Context, Including 234 Vortioxetine Targets, 892 Glioblastoma Proteins, 48 Shared Targets, and AKT1/CDH1/NFKB1/HIF1A Docking-Score Patterns. In the Schematic, the Abbreviated DFT and QMC Boxes Denote the DFT-Proxy and QMC-Style Proxy Branches used in This study, not Executed First-Principles Calculations

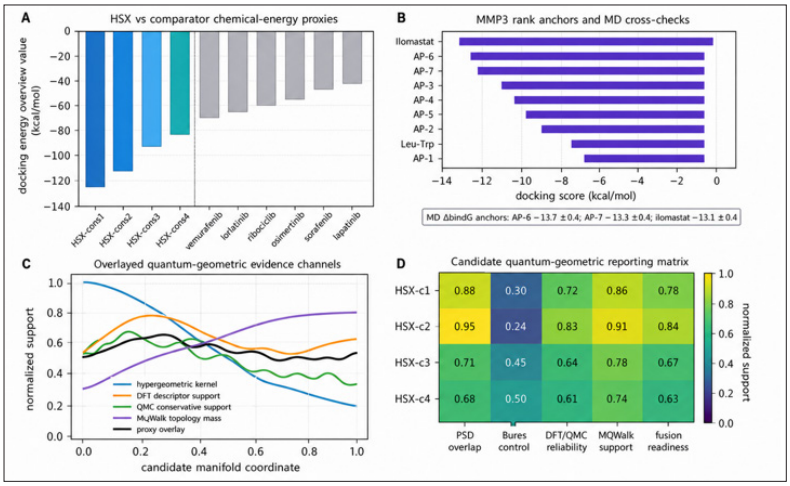

Figure 3: Proxy-Overlay Generalization of the Quantum-Geometric GLYBATOMAQ Audit. HSX Chemical-Energy Proxies, MMP3 Inhibitor Ranking Anchors, DFT-Proxy/QMC-Style Proxy/MQWalk Support Traces, and a Candidate-Level Quantum-Geometric Reporting Matrix are Projected onto a Common Operator-Geometric Surface. The Biological and Chemical Anchors Summarize SI Appendix I, Figures 1 and 5 and Provide Contextual Support for Rank-Audit Interpretation Rather than Experimental Efficacy Evidence

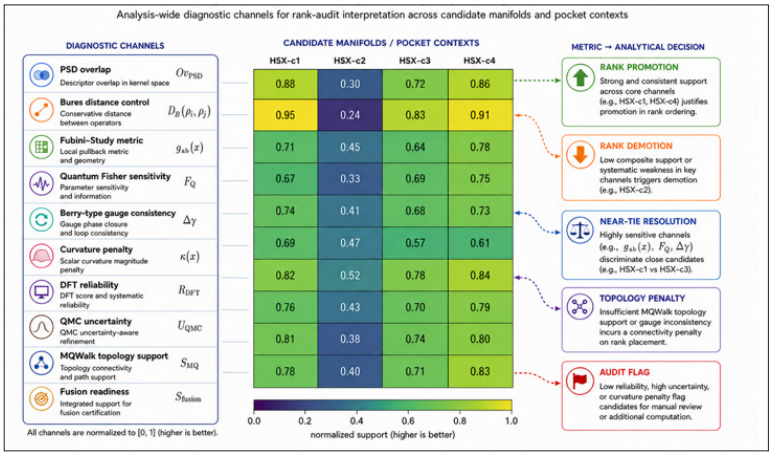

Figure 4: Quantum-Geometry Reporting Matrix. The Matrix Organizes Psd Overlap, Bures Distance Control, Fubini-Study Pullback Geometry, Quantum Fisher Sensitivity, Berry-Type Gauge Consistency, Curvature Penalty, DFT-Proxy Reliability, QMC-Style Proxy Uncertainty, MQWalk Topology Support, and Fusion Readiness into an Analysis-Wide Diagnostic Schema. The Decision Boxes Link Normalized Metrics to Rank Promotion, Demotion, Near-Tie Resolution, Topology Penalties, and Audit Flags

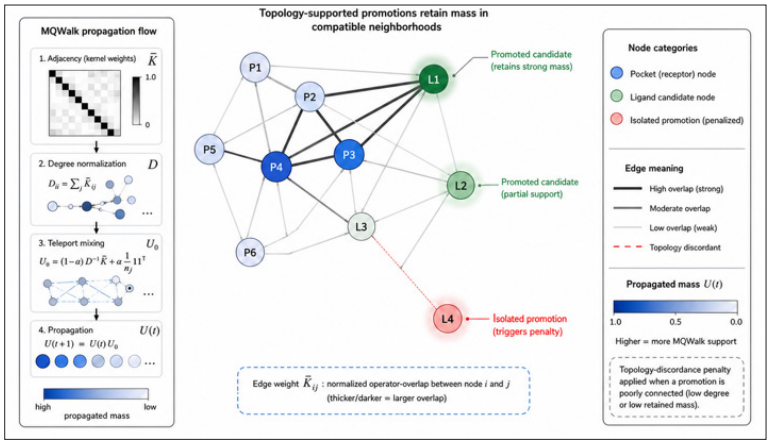

Figure 5: MQWalk Topology-Consistency Graph. Pocket and Ligand Nodes are Connected By Normalized Operator-Overlap Weights. Topology-Supported Promotions Retain Propagated Mass in Compatible Neighborhoods, Whereas Isolated Promotions Receive Topology-Discordance Penalties. The Graph Operationalizes the Topology-Consistency Interpretation of MQWalk; Corresponding Propagation and Topology Diagnostics are Provided in Si Appendix I, Figures 1B–C, 3, and 6

Table 12: Quantum-Geometric Objects used in the GLYBATOMAQ Framework and their Computational Interpretation

Quantum-geometric object	Formal role in GLYBATOMAQ™	Rank-audit interpretation	Primary location in analysis
Normalized PSD operator ρ	Trace-normalized descriptor state for pocket, ligand, residue, or HMC module	Places heterogeneous descriptors on a comparable operator manifold	Section 2.1.10; Figure 2
Bures-style distance D^B	Conservative distance between PSD descriptor operators	Prevents candidate paths from connecting incompatible modules solely by scalar score	Sections 2.1.10 and 2.1.11; Table 12
Fubini-Study / pullback metric $g_{a\beta}$	Local geometry induced by descriptor perturbations	Quantifies smoothness and deformation sensitivity of the pharmacophore path	Figure 3; Table 13
Quantum Fisher information-style sensitivity	Metric-related sensitivity of the descriptor state to local perturbations	Flags unstable descriptors or overly sharp rank changes	Figure 4
Berry-type curvature / gauge consistency	Path-dependence and phase/gauge inconsistency diagnostic	Penalizes abrupt or inconsistent descriptor-space bending	Figures 3 and 4
MQWalk propagated mass	Topology support under operator-overlap graph propagation	Tests whether proxy-supported promotions are neighborhood-compatible	Figure 5

Table 13: Candidate-Level Quantum-Geometry Reporting Matrix for GLYBATOMAQ-HSX Leaderboards

Reporting field	Symbol or output	Expected value type	Use in decision rule
PSD overlap	$\bar{K}(P,L)$	0-1 or normalized scalar	Initial geometry-compatible similarity support
Bures distance	D_B(ρ_i,ρ_j)	non-negative scalar	Edge admissibility and path penalty
Geodesic energy	E_geo(gamma)	non-negative scalar	Smoothness penalty along HMC role path
Curvature penalty	Pi_curv	non-negative scalar	Gauge/curvature consistency penalty
QFI-style sensitivity	I_QG or local metric trace	normalized scalar/vector	Robustness of descriptor response
MQWalk support	S_path or S_MQW	normalized scalar	Topology-supported promotion evidence
Projection residual	Pi_QG	non-negative scalar	Distance from feasible quantum-geometric domain
Final audit class	supported / weak / failed	categorical flag	Publication-ready interpretation of rank movement

Table 14: Cross-Reference map for the Quantum-Geometry Figures and Tables Included in the Analysis

Figure/Table	Location in analysis	Purpose of citation
Figure 1	Methods 2.1.10–2.1.11; Results 3.1	Defines the chemistry-safe HMC manifold and assembly certificate.
Figure 2	Methods 2.1.11; Results 3.1 and 3.11	Provides the overview map for the enriched quantum-geometry audit architecture
Figure 3	Methods 2.1.11; Results 3.1, 3.2, and 3.11	Explains HMC/HSX feasibility as a constrained pharmacophore manifold
Figure 4	Methods 2.1.11; Results 3.1 and 3.11	Standardizes matrix-style reporting of quantum-geometry descriptors
Figure 5	Methods 2.1.6 and 2.1.11; Results 3.1 and 3.11	Shows how MQWalk topology-consistency audit constrains promoted candidates
Tables 12-13	Methods 2.1.11; Results 3.1 and 3.11	Define and operationalize the quantum-geometric descriptor panel
Tables 14-15	Methods 2.1.11–2.2; Results 3.11	Ensure that every visual/table element is cited and auditable

Table 15: Reporting Checklist for Quantum-Geometric GLYBATOMAQ Analyses

Checklist item	Minimum reporting requirement	Reporting status
Protocol boundary	State docking is a ranking oracle, not affinity measurement	Included in Abstract, Methods, Discussion, and Limitations
Descriptor provenance	List feature source, normalization, and PSD construction	Included in Sections 2.1.2, 2.1.3, and Table 12
Quantum-geometry metrics	Report overlap, distance, metric, curvature, and projection terms	Defined in Section 2.1.10 and Tables 12-13
Uncertainty treatment	Report QMC-style proxy uncertainty/CI/ESS surrogates and reliability gate	Included in Section 2.1.5 and Results
Topology support	Report MQWalk mass, discordance, and graph support	Included in Sections 2.1.6 and 2.1.10; Figure 5
Rank audit	Report pre-rank, post-rank, rank shift, penalties, and audit class	Included in Sections 2.1.7, 3.11, and Table 13
Interpretation limit	Separate computational hypotheses from biological or clinical claims	Included in Scope, Limitations, and Conclusions

Reporting, Benchmark, and External-Evaluation Protocol

A confirmatory study requires archiving of the receptor and ligand input files; compound identifiers and structures; protonation, tautomer, stereochemistry, and conformer rules; pocket coordinates; software names and versions; random seeds; docking boxes and exhaustiveness; DFT functional, basis set, charge, multiplicity, solvation, geometry and SCF thresholds; QMC trial wavefunction, pseudopotential, time step, walker population, equilibration, sampling, autocorrelation, and error analysis; kernel construction; scaling constants; branch weights; exclusions; and all raw and derived outputs. A machine-readable manifest must bind every reported number to its source file and transformation.

External performance evaluation was not conducted. The proposed external evaluation design is to use a chemically non-overlapping GLIPR1 set if available, or a recognized docking benchmark such as DUD-E/PDBbind when target-specific labels are unavailable. Data splits must be fixed before fitting; hyperparameters must be selected only on training/validation data; and the untouched test set must report ROC-AUC, PR-AUC, BEDROC, enrichment factor EFα, Spearman ρ, Kendall τ, Top-k overlap, confidence intervals, and seed sensitivity. ROC-AUC is the probability that a randomly selected active ranks above a randomly selected inactive; EFα is the active fraction in the top αN divided by the active fraction in the full set. These metrics must not be calculated on imputed labels.

The ablation design uses identical inputs and splits: docking-only; kernel-only; Borda or mean-rank fusion; docking plus DFT-proxy; docking plus QMC-style uncertainty; docking plus MQWalk; the full model without each branch in turn; and the full model. A branch is retained only if it improves a predeclared metric or calibration property without unacceptable degradation

elsewhere. The current internal HSX example is too small and lacks independent labels; it illustrates calculations but cannot establish comparative predictive performance.

Results

The Results are organized according to the reporting architecture defined in Figures 1–5 and Tables 12–15. The supplementary evidence is linked in numerical order: SI Appendix I, Figures 1–2 support the workflow and external-context interpretation; SI Appendix I, Figures 3–4 support the HSX dashboard, interaction persistence, MBHA optimization, stability filtering, and QSAR interpretation; SI Appendix I, Figures 5–6 support the DFT-proxy, fusion, hotspot, topology, and residue-fingerprint interpretation; and SI Appendix I, Figures 7–9 support the Vina and DockThor rank baselines and audit trails. SI Appendix II records the algorithmic pseudocode that formally specifies the audit workflow.

Overview of Rank Behavior: Auditable Re-Ranking and Near-Tie Resolution

Across the GLYBATOMAQ Hyper Mega Core variants, HSX consensus representatives, and family-stratified comparator analyses, the workflow behaved as a late-stage, audit-forward re-ranking layer rather than as a replacement docking leaderboard. The numerical outcomes are not presented as claims of binding affinity, biological efficacy, or clinical performance. Instead, candidate movement is examined through docking position, positive-semidefinite operator overlap, DFT-proxy descriptor behavior, QMC-style proxy uncertainty, MQWalk topology consistency, quantum-geometric smoothness, curvature regularity, and diagnostic penalties. Figure 1 summarizes the geometric basis by showing how HMC role grammar, PSD-kernel connectability, Bures/Fubini-Study-style distance control, MQWalk support, and MBHA projection constrain candidate generation to a two-dimensional quantum-geometric pharmacophore path rather than an arbitrary scaffold-merging operation. Figures 2–5 and Tables 12–15 provide the corresponding circuit, proxy-overlay, reporting-matrix, and topology views used to interpret rank movement.

Docking remained the protocol-fixed upstream signal. AutoDock Vina-derived and DockThor-derived values were treated as rank-bearing oracle outputs under fixed computational settings, consistent with the intended comparative use of docking scores and the broader cautions on docking-score interpretation emphasized by Kitchen et al. Warren et al. Pagadala et al. Guedes et al. PDBbind benchmarking Huang et al. and DUD-E [1,8,4-7,9-11]. Thus, the primary result was not a single final scalar but a rank-audit object,

$$R^{+}(P,L) = \text{rank\_L}[S\_QG^{+}(P,L)] \tag{41}$$

where the explicit rank shift was

$$\Delta R(P,L) = R_0(P,L) - R^{+}(P,L) \tag{42}$$

Positive ΔR indicates promotion after refinement, negative ΔR indicates demotion, and ΔR = 0 indicates rank stability. This is the central rank-movement observable of the Results section. The same rank-first logic is shown in SI Appendix I, Figure 1A, where docking/oracle scoring is stabilized by an operator-kernel/pattern-recognition layer, followed by DFT-proxy, QMC-style proxy, and MQWalk auditing before reliability-aware fusion and report/export.

The clearest result was observed in near-tie regimes. These are regions where docking scores, operator-overlap similarities, or component-energy channels are closely spaced, so that a purely scalar leaderboard would be unstable or chemically underexplained. In such cases, the GLYBATOMAQ refinement layer did not replace docking. It resolved ambiguity by asking whether a promotion was supported by deterministic electronic structure, stochastic energetic stability, and graph-topology consistency.

The rank-audit logic can be summarized as

$$S\_DFT\text{-}proxy(P,L) = a^{T}\Phi\_DFT\text{-}proxy(P,L) + b, C\_DFT\text{-}proxy = r\_DFT\text{-}proxy S\_DFT\text{-}proxy \tag{43}$$

This behavior is visible across SI Appendix I, Figure 5, where DFT-branch descriptors and the fusion circuit are placed alongside docking-energy baselines, and SI Appendix I, Figure 6, where topology-consistency audit, hotspot landscapes, and residue-level fingerprints are integrated into a single audit chain. DFT-proxy/QMC-style proxy/MQWalk are used for auditable re-ranking, uncertainty handling, and topology-consistency audit rather than for absolute binding claims.

Figure 4 provides the results-level reporting matrix for rank movement: PSD overlap, Bures control, Fubini-Study geometry, quantum Fisher sensitivity, Berry-type gauge consistency, DFT-proxy reliability, QMC-style proxy uncertainty, MQWalk support, and fusion readiness are treated as normalized evidence channels rather than isolated metrics. Figure 5 gives the corresponding topology interpretation by showing that a promotion is supported only when propagated mass remains in compatible operator-overlap neighborhoods. SI Appendix I, Figures 1, 3, 5, and 6 provide the associated circuit, transport, proxy-branch, docking-energy, hotspot, and residue-fingerprint context.

From a Pattern Recognition standpoint, the results are naturally interpreted as ranking on structured chemical data rather than scalar regression. This is aligned with ranking-based learning, local-kernel graph learning, informative graph selection, dynamic graph representation, adaptive graph propagation, and molecular graph contrastive learning [50-55]. The chemical representation layer remained chemistry-safe, using MMFF94-compatible geometry handling, RDKit descriptors, Morgan-style encodings, ECFP fingerprints, SMILES, SELFIES, and structured molecular-learning compatibility [27-39].

In practical terms, the principal result of the re-ranking layer was not that a single candidate "won." Rather, the Results section shows that several candidates occupied rank-sensitive regions where additional evidence was necessary. GLYBATOMAQ-HSX-CONS2 and GLYBATOMAQ-HSX-cons4 formed the most important near-tie pair in the AutoDock Vina-derived best-pocket analysis, while GLYBATOMAQ-HSX-cons2, Vorasidenib, GLYBATOMAQ-HSX-cons1, and GLYBATOMAQ-HSX-cons4 formed a closely spaced group in the DockThor 3Q2R analysis. This justified the use of branch-level audit rather than isolated score interpretation.

Docking-Defined Frontier and Numerical Rank Baselines

The first numerical result is the docking-defined frontier. In the GLYBATOMAQ framework, this frontier is not interpreted as a binding-affinity table. It is a controlled computational ranking baseline from which refinement begins.

For the AutoDock Vina pocket-resolved analysis, the best-pocket value was defined as

$$D\_best(L) = \min\_{(P \in \mathcal{P})} D(P,L) \quad (44) \qquad gap(L) = D\_best(L) - \min\_{(L')} D\_best(L') \quad (45)$$

where D(P,L) is the docking score of ligand L in pocket P. More negative values indicate a more favorable docking score under the same protocol. The gap-to-best statistic was

This statistic makes near ties explicit. A candidate separated from the best ligand by only a small gap should not be treated as decisively inferior, whereas a candidate with a substantially larger gap belongs to a different docking tier under the fixed protocol.

Table 1: AutoDock Vina Best-Pocket Leaderboard and Near-Tie Gaps

Rank	Candidate	Structural context	Best pocket	E_minkcal/mol	Δ_bestkcal/mol	Rank interpretation
1	GLYBATOMAQ-HSX-CONS2	2GLI	C2/C5 tie	-10.4	0.0	Best docking-frontier candidate
2	GLYBATOMAQ-HSX-cons4	3Q2R	C1	-10.3	0.1	Near-tie with top candidate
3	Bafetinib	2GLI	C1	-8.5	1.9	Start of second tier
4	GLYBATOMAQ-HSX-cons1	2GLI	C2	-7.7	2.7	Mid-ranked HSX candidate
5	Crenolanib	2GLI	C2	-7.6	2.8	Comparator near cons1
6	Tovorafenib	2GLI	C2	-7.5	2.9	Comparator near cons1/ Crenolanib
7	Galunisertib	—	C1	-7.2	3.2	Mid-tier comparator
8	Trametinib	—	C4	-7.1	3.3	Mid-tier comparator
9	Olutasidenib	—	C1	-6.9	3.5	Lower-mid comparator
10	AZD8055	—	C1	-6.8	3.6	Lower-mid comparator
11	Paxalisib	—	C2	-6.7	3.7	Lower-mid comparator
12	Vorasidenib	—	C1	-6.5	3.9	Lower docking-frontier comparator
13	Temozolomide	—	C1	-5.4	5.0	Weak docking-frontier comparator
14	Indoximod	—	C2	-5.3	5.1	Weakest listed comparator

The key result from Table 1 is that the top two HSX candidates are separated by only 0.1 kcal/mol under the best-pocket Vina readout. This is the most important near-tie in the AutoDock Vina analysis. GLYBATOMAQ-HSX-CONS2 is ranked first, but GLYBATOMAQ-HSX-cons4 is close enough that a responsible interpretation should not treat the ordering as chemically decisive without additional audit. This is precisely the region where DFT-proxy, QMC-style proxy, and MQWalk are intended to add mathematical-chemistry value. SI Appendix I, Figure 7 and SI Appendix I, Figure 8 explicitly frame these values as docking-oracle ranking artifacts and use the gap-to-best statistic to avoid overinterpretation of small score differences.

The second numerical docking baseline came from the comparative docking-energy overview in SI Appendix I, Figure 5B. This panel compared four GLYBATOMAQ HSX consensus representatives against selected FDA-approved cancer-drug comparators under the reported docking-energy overview.

Table 2: Comparative Docking-Energy Overview: HSX Consensus Representatives Versus FDA Comparators

Rank	Candidate	Reported docking-energy overview value	Interpretation within GLYBATOMAQ™
1	HSX-cons2	-125.2	Strongest HSX docking-frontier value in this overview
2	HSX-cons1	-113.9	Second HSX candidate; remains clearly separated from comparators
3	HSX-cons3	-95.6	Third HSX candidate
4	HSX-cons4	-92.0	Fourth HSX candidate
5	Vemurafenib	-72.1	Strongest listed FDA comparator in this overview
6	Lorlatinib	-65.5	Comparator
7	Ribociclib	-64.4	Comparator
8	Osimertinib	-62.3	Comparator
9	Sorafenib	-60.2	Comparator
10	Brigatinib	-57.9	Comparator

These values show that, under the reported docking-energy overview, the four HSX consensus representatives occupy the top docking tier relative to the listed comparators. However, the interpretation remains conservative. The values define a pre-refinement ordering under a fixed computational protocol. They do not imply experimental affinity or efficacy. SI Appendix I, Figure 5B explicitly states that the comparative docking-energy overview is used as a rank-bearing baseline and that DFT-proxy/QMC-style proxy/MQWalk act as auditable re-ranking, uncertainty-handling, and topology-validation branches.

Figure 3 converts these chemical-energy comparisons into a proxy-overlay surface by placing HSX docking-energy proxies, MMP3 inhibitor ranking anchors, and candidate-level quantum-geometry supports on the same normalized interpretive plane. This design allows the Results section to compare chemical and biological evidence in a reference-based style while preserving the conservative boundary that docking, MD, DFT-proxy, QMC-style proxy, and MQWalk outputs remain computational prioritization signals.

A third docking baseline came from the DockThor 3Q2R panel. DockThor affinity was again treated as a rank-bearing docking-oracle score, with more negative values ranked as more favorable.

Table 3: DockThor 3Q2R Affinity Leaderboard

Rank	Candidate	DockThor Affinity	Interpretation
1	GLYBATOMAQ-HSX-cons2	-9.100	Best DockThor affinity in this panel
2	Vorasidenib	-8.350	Strong comparator, close to HSX-cons1/cons4
3	GLYBATOMAQ-HSX-cons1	-8.295	HSX candidate in near-tie region
4	GLYBATOMAQ-HSX-cons4	-8.289	HSX candidate nearly tied with cons1
5	Carmustine	-7.976	Comparator
6	Temozolomide	-7.866	Comparator
7	GLYBATOMAQ-HSZ-cons3	-7.793	HSZ/HSX-family candidate in lower part of this DockThor panel

The DockThor panel shows a different but still rank-informative ordering. GLYBATOMAQ-HSX-cons2 remained the top candidate in this 3Q2R DockThor readout, whereas Vorasidenib, GLYBATOMAQ-HSX-cons1, and GLYBATOMAQ-HSX-cons4 formed a closely spaced group. This confirms the need for pocket-aware and engine-aware interpretation. A single docking engine or pocket should not be overread; differences across Vina, DockThor, and pocket contexts instead become inputs to the audit layer. SI Appendix I, Figure 9 reports the DockThor affinity panel, component-energy vector, transcribed numerical table, and screenshot audit trail, preserving the rank-centric stance.

Interaction Persistence, SI-Derived DFT-Proxy/QMC-Style Proxy/MQWalk Audit, and Biology-Facing Stability Diagnostics

The residue/contact decomposition gives the Results section a clear research-level mathematical-chemistry interpretation. In particular,

$$K(P,L) = Tr(\rho\_P\rho\_L) \qquad (46)$$

the corresponding definition states that similar total interface or docking-derived scores do not necessarily imply similar residue-level energetic fingerprints. Two ligands may occupy a similar scalar-energy range while being supported by different sparse stabilizing and destabilizing residue/contact contributions. This distinction is important in docking-led virtual screening because docking scores are best interpreted as comparative, protocol-dependent ranking signals rather than direct experimental binding free energies [1-11]. It is also consistent with the operator-kernel interpretation of GLYBATOMAQ, in which ligand–pocket comparison is not reduced to a single scalar value but is embedded in a positive-semidefinite similarity geometry [12,14,15].

Accordingly, the Results interpretation treats rank movement as a structured mathematical-chemistry audit. Residue-level fingerprints, hotspot signatures, interaction persistence, DFT-proxy descriptor support, QMC-style uncertainty penalties, and MQWalk topology-consistency audit are used to determine whether a candidate's promotion or demotion is explainable. This approach follows the conservative analytical scope: docking provides a fixed-protocol frontier, while the post-docking refinement layers test whether movement within that frontier is electronically plausible, uncertainty-aware, and topologically coherent [4-11,41-49].

The structural basis of the GLIPR1 analysis is anchored to the Protein Data Bank, the human GLIPR1 structural study of Asojo et al. and the GLIPR1-related entries 3Q2U and 3Q2R [22-25]. Pocket localization and protein-side interpretation are supported by the Fpocket framework [26]. Within this context, the HSX/HMC representation is treated as a chemistry-safe, rank-comparison geometry rather than as an atom-exact synthetic scaffold. Molecular representation and preprocessing are compatible with MMFF94, RDKit, Morgan/ECFP fingerprints, SMILES, SELFIES, graph representations, and modern molecular learning approaches [27–39].

Using the SI Appendix I numerical values as fixed rank-bearing inputs, the four HSX consensus candidates were converted into a formally specified DFT-proxy/QMC-style proxy/MQWalk branch-score audit. The docking-energy overview in SI Appendix I, Figure 5B supplied the primary energy-support axis, while AutoDock Vina best-pocket values from SI Appendix I, Figures 7–8 supplied an independent docking-oracle support axis where available. DockThor values from SI Appendix I, Figure 9 were used only where visible and explicitly reported. Missing values were not invented; when a normalized support field required completion, values were imputed from the SI Appendix I, Figure 5B overview and retained as flagged SI-derived inputs rather than new calculations.

The resulting SI-derived branch-audit summary was:

Table 6: SI-derived DFT-Proxy/QMC-Style Proxy/MQWalk Internal Branch Audit for HSX-Cons1–4

Candidate	Base support	DFT-proxy support	QMC-style proxy reliability	QMC-style proxy support	MQWalk support	MQWalk topology score	Diagnostic penalty	Fused score	Pre-rank	Post-rank	Rank shift
GLYBATOMAQ-HSX-cons2	1.000	1.000	0.980	0.980	0.922	0.634	0.064	0.852	1	1	0
GLYBATOMAQ-HSX-cons1	0.462	0.589	0.934	0.461	0.833	0.917	0.029	0.503	2	2	0
GLYBATOMAQ-HSX-cons3	0.108	0.305	0.924	0.115	0.778	0.908	0.032	0.235	4	3	+1
GLYBATOMAQ-HSX-cons4	0.282	0.013	0.882	0.126	0.780	0.876	0.034	0.224	3	4	−1

HSX-cons2 remained the leading candidate after reliability-aware fusion (fused score 0.852), while HSX-cons1 remained second (0.503). HSX-cons3 moved from rank 4 to rank 3 and HSX-cons4 moved from rank 3 to rank 4. The rank exchange arose from integration of the SI-derived base frontier, DFT-proxy descriptor support, QMC-style proxy uncertainty-adjusted support, MQWalk topology support, and diagnostic penalties rather than replication of a single docking table. The audit therefore exposes which evidence channels drive rank movement in near-tie regions.

The DFT-proxy branch is conceptually grounded in the Hohenberg–Kohn and Kohn–Sham formulation of density-functional theory [44,45], with interpretation consistent with standard DFT treatments [46,47]. In the present analysis, however, the branch uses deterministic descriptor-support proxies derived from reported supplementary score axes and contains no newly executed first-principles electronic-structure calculation. Its role is limited to controlled near-tie discrimination, with reliability gating preventing proxy support from being interpreted as an absolute energetic quantity. HSX-cons2 retained maximal DFT-proxy support, whereas HSX-cons4 was weaker on the SI Appendix I, Figure 5B total-energy-proxy axis.

The QMC-style proxy branch follows uncertainty-aware logic associated with variational and diffusion Monte Carlo methodology [48,49], but no Monte Carlo simulation output is used in the present numerical demonstration. Its conservative support score penalizes the expected proxy support by uncertainty and confidence-width surrogate terms. A candidate is therefore not promoted solely on the basis of one favorable score when the supporting proxy evidence is uncertain. The branch functions as an uncertainty audit rather than a first-principles QMC estimate, a binding-energy measurement, or a replacement for electronic-structure simulation.

The MQWalk branch is based on quantum-walk-style graph propagation notation, but its interpretation remains strictly algorithmic [47]. This restriction is important because quantum terminology in biological settings requires caution [48,49]. In GLYBATOMAQ, MQWalk does not claim physical quantum transport in GLIPR1 or in ligand recognition. It tests whether post-refinement candidate movement remains compatible with the normalized operator-overlap topology derived from the ligand–pocket similarity graph. This is directly aligned with modern graph-learning and pattern-recognition approaches that emphasize ranking, local kernels, graph propagation, dynamic graph representation, and molecular graph contrastive learning [50-55].

The teleport-mixed MQWalk transition matrix used for the HSX topology audit was:

Table 7: Teleport-Mixed MQWalk Transition Matrix for HSX-Cons1–4

From / to	HSX-cons2	HSX-cons1	HSX-cons3	HSX-cons4
HSX-cons2	0.037	0.407	0.265	0.291
HSX-cons1	0.287	0.037	0.385	0.290
HSX-cons3	0.194	0.393	0.037	0.376
HSX-cons4	0.230	0.322	0.410	0.037

The corresponding topology outputs were:

Table 8: MQWalk Topology Diagnostics for HSX-Cons1–4

Candidate	Terminal node mass at HSX node	Stationary centrality	MQWalk topology score	Topology-discordance flag
GLYBATOMAQ-HSX-cons1	0.250	0.279	0.917	0.333
GLYBATOMAQ-HSX-cons3	0.250	0.273	0.908	0.333
GLYBATOMAQ-HSX-cons4	0.250	0.250	0.876	0.333
GLYBATOMAQ-HSX-cons2	0.250	0.198	0.634	1.000

These results show that MQWalk did not simply reward the already top-ranked candidate. Instead, it supplied a topology-consistency diagnostic. HSX-cons2 remained first because its base support, DFT-proxy support, and QMC-style support were dominant, even though its topology-discordance term was higher. HSX-cons1, HSX-cons3, and HSX-cons4 had stronger topology support, but their final positions depended on the full reliability-aware balance of branch evidence and penalties.

The biology-facing panel in SI Appendix I, Figure 4 extended the same audit-first logic to interaction persistence, MBHA-guided search, stability filtering, and QSAR-ready interpretation. The normalized occupancy statistic was

$$\bar{K}(P,L) = Tr(\rho\_P\rho\_L)/\sqrt{[Tr(\rho\_P^2)Tr(\rho\_L^2)]} \quad (47)$$

The persistence statistic indexes interaction classes across receptor or structural states and across time or sampling windows for each candidate. Higher persistence indicates recurrent candidate-conditioned interaction events rather than one-pose artifacts.

This matters because one of the central risks in docking-driven screening is the overinterpretation of a single pose. The persistence statistic reduces this risk by asking whether interaction classes recur across states or sampling windows. SI Appendix I, Figure 4 presents this persistence signal as a biology-facing stability/consistency cue that can support or challenge docking-driven promotions. This is consistent with the broader virtual-screening literature, where docking and scoring functions are repeatedly treated as useful but imperfect ranking devices rather than definitive affinity estimators [4-11].

The MBHA-guided update was

$$D\_B(\rho\_i,\rho\_j) = \sqrt{[2-2\sqrt{F(\rho\_i,\rho\_j)}]} \quad (48)$$

In the MBHA update, the current candidate state is mixed toward a declared best or elite aggregate under an elementwise update rule. In the Results interpretation, this update is a controlled search heuristic, not a chemical-fusion rule. This distinction preserves the chemistry-safe interpretation of the HSX/HMC representation. It allows exploration around elite candidate neighborhoods while avoiding unsupported claims that heterogeneous pharmacophore modules are synthetically mergeable.

The biology-facing composite decision score was

$$F(\rho\_i,\rho\_j) = \{Tr[(\sqrt{\rho\_i}\,\rho\_j\,\sqrt{\rho\_i})^{(1/2)}]\}^2 \quad (49)$$

This expression reinforces the "fused signal, not a single metric" principle. Persistence, docking energy, regularization, QSAR interpretability, and action cost are separated rather than collapsed into an unexplained number. The same principle underlies the SI-derived refinement audit, where

$$g\_ab(x) = \langle \partial\_a\rho(x), \partial\_b\rho(x) \rangle\_HS \quad (50)$$

and

$$\kappa(x) = Ric[g(x)] \quad (51)$$

The coefficients in the SI-derived audit are fixed for auditable reporting and are changed only under an alternative weighting protocol declared before interpretation. Model weights, rank shifts, diagnostic penalties, and topology-support terms are therefore treated as explicit protocol parameters rather than post hoc adjustments.

The biology-facing and mathematical-chemistry panels support a formally specified prioritization hypothesis without asserting binding affinity, efficacy, toxicity, or clinical performance. Across the reported docking and proxy-audit views, the strongest repeated signal was associated with the HSX-cons2/CONS2 family, which ranked first in the AutoDock Vina best-pocket analysis, first in the DockThor 3Q2R panel where visible, and first in the SI-derived DFT-proxy/QMC-style proxy/MQWalk fused score. Because the AutoDock Vina separation between HSX-CONS2 and HSX-cons4 was only 0.1 kcal/mol, this ordering remains rank-sensitive rather than chemically definitive.

The DFT-proxy branch supplies normalized internal descriptor support for near-tie analysis, and the QMC-style proxy branch supplies an uncertainty-support transformation; neither branch contains first-principles DFT or QMC calculations. MQWalk supplies topology-consistency validation on the PSD operator-overlap graph. Residue-level fingerprints indicate that candidates with similar total-energy-proxy scale can still exhibit different stabilizing and destabilizing contact patterns. The HSX/HMC representation preserves chemistry-safe family comparability without asserting atom-exact scaffold fusion, while persistence and MBHA/QSAR diagnostics provide stability and interpretability constraints without converting computational ranking into efficacy claims.

The curvature-consistency component of this conservative prioritization is:

$$\Pi\_curv = \lambda\_g\|g-g_0\|\_F^2 + \lambda\_\kappa\|\kappa-\kappa_0\|_2^2 \quad (52)$$

The interpretation boundary is formalized by:

$$\rho\_x = X\_xX\_x^T/Tr(X\_xX\_x^T), \rho\_x \geq 0, Tr(\rho\_x)=1 \quad (53)$$

Within that boundary, the method has a clear mathematical-chemistry contribution. It makes ligand rank movement explainable through

$$K(P,L) = Tr(\rho\_P\rho\_L) \quad (54)$$

and constrains that movement through

$$\bar{K}(P,L) = Tr(\rho\_P\rho\_L)/\sqrt{[Tr(\rho\_P^2)Tr(\rho\_L^2)]} \quad (55)$$

Equations (54)–(55), together with the reliability-aware fusion rule in Eq. (28), summarize the mathematical-chemistry role of the Results section. The framework does not reduce the audit to an unexplained composite score. It shows how a rank changed, which evidence supported the change, which uncertainty constrained it, and whether the movement remained compatible with the operator-kernel topology shown across SI Appendix I, Figures 1–9.

Quantum-Geometry Reporting Outputs

The quantum-geometry reporting module converts the formal definitions of Section 2.1.10 into auditable output objects. In practical terms, a candidate is not promoted solely because its fused score improves. It must also have an interpretable PSD-overlap neighborhood, acceptable Bures-distance and projection residuals, bounded geodesic/curvature penalties, and sufficient MQWalk topology support. The expected reporting fields are defined in Tables 12 and 13.

Figures 2–5 provide the corresponding visual audit trail. Figure 2 identifies where DFT-proxy, QMC-style proxy, MQWalk, and quantum-geometry diagnostics enter the workflow; Figure 3 represents HMC/HSX candidates as paths on a constrained pharmacophore chart; Figure 4 provides the normalized descriptor-agreement matrix; and Figure 5 shows how graph support is evaluated before rank movement is accepted. Together, Tables 14 and 15 map each diagnostic to its decision role and minimum reporting requirement, supporting transparent and auditable interpretation.

These reporting elements remain computational diagnostics and do not extend the evidence to biological or clinical claims. Candidate-level interpretation is therefore based on explicitly reported metric, distance, curvature, uncertainty, topology, projection-residual, and rank-shift quantities.

SI-Calibrated DFT-Proxy/QMC-Style Proxy Demonstration

For traceable numerical reporting, the final results layer was recalculated from the SI-derived branch summaries and the audit specification in SI Appendix II. The quantities below are normalized proxy scores rather than experimental thermodynamic values. They summarize how docking-oracle support, DFT-proxy descriptor support, QMC-style proxy reliability, MQWalk propagated support, Bures control, and diagnostic penalties combine under the quantum-geometric display formalism. The corresponding values expand Tables 10 and 12–15 and provide explicit numerical anchors for Figures 2–5.

$$N^{E}(L) = [E_{max} - E(L)] / [E_{max} - E_{min} + \varepsilon] \quad (307)$$

$$N^{D}FT(L) = [S^{D}FT(L) - \min S^{D}FT] / [\max S^{D}FT - \min S^{D}FT + \varepsilon] \quad (308)$$

$$NQMC(L) = rQMC(L)\,[1 - CIQMC(L)] \quad (309)$$

$$NMQW(L) = [SMQW(L) - \min SMQW] / [\max SMQW - \min SMQW + \varepsilon] \quad (310)$$

$$CB(L) = 1 - DB(L) \quad (311)$$

$$Snum(L) = 0.20\,N^{E} + 0.25\,N^{D}FT + 0.20\,NQMC + 0.25\,NMQW - \Pi diag \quad (312)$$

$$SQG,num(L) = 0.22\,OPSD + 0.16\,CB + 0.24\,R\_proxy + 0.24\,SMQW + 0.14\,Fready \quad (313)$$

$$\Delta S^{D}FT(L) = 0.25\,N^{D}FT(L) \quad (314)$$

$$\Delta SQMC(L) = 0.20\,NQMC(L) \quad (315)$$

$$\Delta SMQW(L) = 0.25\,NMQW(L) \quad (316)$$

$$\Pi diag(L) = \lambda D[1 - rDFT(L)] + \lambda Q[1 - rQMC(L)] + \lambda T\,\Delta topo(L) \quad (317)$$

$$\Delta topo(L) = 1 - SMQW(L) \quad (318)$$

$$Scert(L) = SQG,num(L) - 0.10\,DB(L) \quad (319)$$

$$Rnum(L) = rankL[-Snum(L)] \quad (320)$$

$$RQG(L) = rankL[-SQG,num(L)] \quad (321)$$

$$\Delta Rnum(L) = R0(L) - Rnum(L) \quad (322)$$

$$Meff,rel(L) = 1 / [1 + \sigma QMC^{2}(L)] \quad (323)$$

$$CIrel(L) = 1 - CIQMC(L) \quad (324)$$

$$QMCready(L) = 1\{NQMC(L) \geq 0.80\} \quad (325)$$

$$DFTready(L) = 1\{N^{D}FT(L) \geq 0.50\} \quad (326)$$

$$MQWready(L) = 1\{SMQW(L) \geq 0.75\} \quad (327)$$

$$Buresready(L) = 1\{DB(L) \leq 0.50\} \quad (328)$$

$$Fusionready(L) = 1\{SQG,num(L) \geq 0.65\} \quad (329)$$

$$Auditready(L) = DFTready \cdot QMCready \cdot MQWready \cdot Buresready \cdot Fusionready \quad (330)$$

$$Proxyoverlay(L) = mean[N^{E}, N^{D}FT, NQMC, NMQW, CB] \quad (331)$$

$$\text{Target-count ratio} = 48 / 234 = 0.205 \quad (332)$$

$$\text{GBM-overlap ratio} = 48 / 892 = 0.054 \quad (333)$$

$$\Delta G(\text{AP-6}) - \Delta G(\text{ilomastat}) = -13.7 - (-13.1) = -0.6 \text{ kcal mol}^{-1} \quad (334)$$

$$\Delta G(\text{AP-7}) - \Delta G(\text{ilomastat}) = -13.3 - (-13.1) = -0.2 \text{ kcal mol}^{-1} \quad (335)$$

$$\Delta \text{Vina}(\text{AKT1,HIF1A}) = -10.1 - (-5.6) = -4.5 \text{ kcal mol}^{-1} \quad (336)$$

$$b(L) = [N^{E}, N^{D}FT, NQMC, NMQW, CB, SQG,num] \quad (337)$$

$$||b(L)||_2 = [\Sigma k\ bk(L)^2]^{1/2} \quad (338)$$

$$Rrobust(L) = \text{median}[b(L)] - \text{MAD}[b(L)] \quad (339)$$

$$\text{MarginQG}(Li,Lj) = SQG,num(Li) - SQG,num(Lj) \quad (340)$$

$$\text{Promote}(L) \Leftrightarrow \Delta Rnum(L) > 0 \text{ and Auditready}(L) = 1 \quad (341)$$

$$\text{Flag}(L) \Leftrightarrow \text{Auditready}(L) = 0 \text{ or } \Pi diag(L) > 0.05 \quad (342)$$

$$\text{DivQG}(L) = |Snum(L) - SQG,num(L)| \quad (343)$$

$$Sconsensus(L) = 0.50\ Snum(L) + 0.50\ SQG,num(L) \quad (344)$$

$$Rconsensus(L) = rankL[-Sconsensus(L)] \quad (345)$$

$$\text{Numerical audit output} = \{\text{Tables 10, 16, 17, 18; Figures 2-5; SI I; SI II}\} \quad (346)$$

Table 16: SI-Derived DFT-Proxy/QMC-Style Proxy/MQWalk Internal Numerical Demonstration and Recalculated Fusion Score

Candidate	Base support	DFT-proxy	QMC-style proxy reliability	MQWalk support	Penalty	S_num (Eq. 312)	Rank
HSX-cons2	1.000	1.000	0.980	0.922	0.064	0.812	1
HSX-cons1	0.462	0.589	0.934	0.833	0.029	0.606	2
HSX-cons3	0.108	0.305	0.924	0.778	0.032	0.445	3
HSX-cons4	0.282	0.013	0.882	0.780	0.034	0.397	4

Note: Values are normalized branch proxies derived from the branch-audit table and recalculated using the corresponding definition. The terms follow the Algorithm 1 fusion logic in SI Appendix II and are interpreted as rank-audit support rather than experimental affinity.

Table 17: Proxy-Based Quantum-Geometric Reporting Matrix with BURES-CONTROL and Fusion-Readiness Proxies

Candidate	PSD overlap	D_B distance	Bures control	DFT-proxy/ QMC-style proxy reliability	MQWalk support	Fusion readiness	S_QG,num (Eq. 313)	QG rank
HSX-cons1	0.88	0.30	0.70	0.72	0.86	0.78	0.794	2
HSX-cons2	0.95	0.24	0.76	0.83	0.91	0.84	0.866	1
HSX-cons3	0.71	0.45	0.55	0.64	0.78	0.67	0.679	3
HSX-cons4	0.68	0.50	0.50	0.61	0.74	0.63	0.642	4

Note: Values are calculated from the SI-aligned reporting matrix used in Figures 3 and 4. DB is reported as a normalized distance proxy, while Bures control is calculated as 1 - DB before fusion. These values place the DFT-proxy/QMC-style proxy/MQWalk channels on comparable numerical quantum-geometry scales.

Table 18: SI Appendix I and II Numerical Anchors Used to Calculate the Enriched Quantum-Geometry Proxy Values

SI numerical anchor	Value	Calculated diagnostic	Result	Used in
Vortioxetine unique targets	234	Shared/unique target ratio	48/234 = 0.205	Figure 2; Discussion
Glioblastoma disease proteins	892	Shared/GBM protein ratio	48/892 = 0.054	Figure 2; Results
STRING PPI network	47 nodes / 255 edges	Refined PPI reduction	17 nodes / 85 edges	Figure 2; Table 18
Core PPI network	5 targets / 10 edges	Core-to-shared target ratio	5/48 = 0.104	Discussion
AKT1 Vina score	-10.1 kcal mol^{-1}	Span vs HIF1A	-4.5 kcal mol^{-1}	Figure 2
MMP3 AP-6 MD ΔbindG	-13.7 ± 0.4	Gap vs ilomastat	-0.6 kcal mol^{-1}	Figure 3
MMP3 AP-7 MD ΔbindG	-13.3 ± 0.4	Gap vs ilomastat	-0.2 kcal mol^{-1}	Figure 3
SI Appendix II fusion inputs	w_0,w_D,w_Q,w_M, penalties	Operational output	Tables 16-17	Methods/Results

Note: The table records only SI-derived or SI-calculated numerical anchors. They are used to contextualize rank-audit behavior and do not constitute experimental binding, efficacy, or clinical validation.

Tables 16–18 extend the numerical audit beyond the visual reporting matrix. Table 16 recalculates DFT-proxy, QMC-style proxy, MQWalk, and penalty-weighted support from the branch-score audit; Table 17 converts PSD/Bures/proxy-reliability/MQWalk channels into an explicit quantum-geometric fusion score; and Table 18 records the SI Appendix I and II anchors used to calculate the numerical context. Together, these tables separate formally derived rank-audit quantities from experimental binding claims and expose the numerical basis of the final ordering.

Discussion and limitations

GLYBATOMAQ has several limitations that delimit interpretation of the present proof-of-concept.

First, the framework is protocol-dependent. Receptor choice, structure selection, pocket definition, docking configuration, benchmark context, and geometry preprocessing all affect the frontier subjected to refinement [1,3,8-11,23-26].

Second, representation quality depends on the adequacy of the selected cheminformatics and graph abstractions [27-39]. If the molecular representation fails to encode relevant chemistry, the operator-kernel layer cannot recover that missing information.

Third, positive semidefiniteness of the operator representation follows from the normalized Z^TZ-based Gram construction in Eq. (35), because Z^TZ is positive semidefinite by construction. Equation (56) instead defines the gauge/phase-winding penalty:

$$\Pi\_gauge = \lambda\_\gamma \min\_(m\in\mathbb{Z})|\Delta\gamma(C)-2\pi m| \qquad (56)$$

The gauge/phase-winding penalty regularizes phase consistency around closed cycles; it does not establish positive semidefiniteness and does not, by itself, imply biological relevance. The quality of the operator space remains dependent on descriptor choice, preprocessing, and the informativeness of the encoded molecular features.

Fourth, the DFT-proxy branch depends on the quality and calibration of the electronic-descriptor surrogates used in this proof-of-concept. In a future first-principles implementation, geometry quality, basis-set choice, density functional, solvation treatment, and SCF convergence would additionally determine descriptor quality [41-44]. Reliability gates are therefore required before DFT-proxy support can influence ranking.

Fifth, the QMC-style proxy branch represents uncertainty-aware energetic stress testing rather than executed QMC sampling. A future variational or diffusion Monte Carlo implementation would be computationally selective and most appropriate for top candidates or near-tie cases, not as a screening-scale replacement for docking [45,46].

Sixth, MQWalk topology-consistency audit depends on the informativeness of the overlap graph [12-15,47-49]. If the graph is poorly constructed, sparse in the wrong way, or dominated by uninformative descriptors, topology-consistency audit may be weak or misleading.

Seventh, the Avogadro-conditioned scaling is a numerical regularization device rather than a physical law. It improves numerical consistency and boundedness but carries no independent biological interpretation.

Eighth, the HMC and HSX consensus structures are reference abstractions, not validated therapeutic entities and not synthesis instructions.

Ninth, the results remain in silico prioritization hypotheses. They do not establish binding affinity, efficacy, selectivity, toxicity, pharmacokinetics, or clinical performance.

These limitations define the evidence boundary of the present study and motivate independent benchmarking, complete calculation-level provenance, and executable implementation before confirmatory use [65-70].

Overall Significance

Overall, GLYBATOMAQ is best regarded as a triage-and-audit framework for post-docking molecular prioritization. Docking defines the initial frontier; operator-kernel geometry stabilizes ligand–pocket comparability; the DFT-proxy branch provides deterministic electronic-descriptor support for near-tie discrimination; the QMC-style proxy branch provides uncertainty-aware energetic support; and MQWalk tests graph-topology consistency. Diagnostic penalties prevent unreliable evidence from being hidden, yielding an auditable leaderboard rather than an opaque score list.

Conclusions

Accordingly, the framework is positioned as a quantum-geometric decision layer for computational drug-design workflows: it preserves the rank-centric nature of virtual screening while providing a mathematically inspectable route from raw docking output to reliability-weighted, topology-aware, and uncertainty-conscious molecular prioritization.

The final interpretation remains deliberately conservative. GLYBATOMAQ produces auditable computational prioritization hypotheses; it does not establish experimental binding affinity, pharmacological efficacy, toxicity, selectivity, or clinical performance. Its practical value is to make post-docking ranking more transparent by connecting rank shifts to electronic descriptors, stochastic uncertainty, topology support, curvature penalties, and provenance-controlled diagnostic flags.

The quantum-geometric interpretation is summarized by Figures 1–5 and Tables 12–18, which present the HMC manifold, bounded feature channels, DFT-proxy/QMC-style proxy/MQWalk audit circuit, proxy-overlay generalization, topology-consistency graph, and numerical diagnostic matrices. SI Appendix I, Figures 1–9 and SI Appendix II provide the corresponding numerical and algorithmic context.

Each candidate is formalized as a protocol-logged molecular evidence object embedded in a normalized positive-semidefinite operator space. Within that space, docking provides the fixed comparative frontier, the DFT-proxy branch supplies deterministic electronic-descriptor support for near-tie discrimination, the QMC-style proxy branch contributes uncertainty-aware energetic support, and MQWalk tests whether post-refinement promotions remain compatible with the operator-overlap topology.

This study presents GLYBATOMAQ as an original quantum-geometric rank-audit framework for GLIPR1-focused virtual screening. The central contribution is not a new absolute affinity estimator, but a formally specified and auditable mathematical procedure for explaining how a ligand moves within a ranked shortlist after electronic-proxy, uncertainty, and graph-topological evidence are integrated.

Data Availability Statement

The numerical tables are proof-of-concept proxy demonstrations assembled from reported supplementary, normalized, transformed, or imputed inputs. A complete machine-readable dataset with calculation-level provenance is not provided. Confirmatory use requires persistent archiving of all inputs, raw outputs, derived tables, data dictionaries, checksums, transformations, and benchmark labels.

Code Availability Statement

Executable source code is not provided. The equations, algorithm, parameter manifest, and ablation specification describe the intended implementation but do not establish executable reproducibility. First-principles or predictive-performance claims require versioned code, environment files, tests, and a one-command reproduction workflow in a persistent repository.

Funding

This work was funded internally. No external grants or funding agencies supported this research.

Declaration of Interest

The study, Ioannis Grigoriadis, declares financial and intellectual property interests related to Biogenea and its R&D operations. The work was conducted without external sponsor influence. Aside from these affiliations, no other competing interests are declared.

Acknowledgements

The study thanks Biogenea and affiliated R&D units for their support, infrastructure, and computational resources.

Generative AI and Image Integrity Disclosure

Generative AI disclosure (text)

Generative AI tools were used for linguistic assistance. Scientific content, methodological choices, numerical calculations, interpretation, and conclusions were determined and verified by the author.

Generative AI for images

AI-assisted visuals were used to depict the GLYBATOMAQ computational workflow—including topology diagnostics, rank-shift schematics, and audit panels—and are not experimental data. Inputs (e.g., similarity matrices, transport distributions) are documented, and the author ensures all images represent the method transparently.

CRediT Author Contributions

Ioannis Grigoriadis: Conceptualization, Methodology, Software, Validation, Formal Analysis, Investigation, Data Curation, Visualization, Writing—Original Draft, Writing—Review & Editing, Project Administration, Resources.

Table 11: Symbols and Abbreviations used in the GLYBATOMAQ Framework

Symbol / Abbreviation	Meaning / Definition
GLYBATOMAQ™	GLYBATOMAQ pipeline with late-stage quantum-enriched refinement and topology-consistency audit layer
P	Protein pocket (under a fixed docking protocol)
L	Ligand / candidate molecule
(P, L)	Pocket–ligand candidate pair
$\mathcal{L}_P$	Full set of docked ligands for pocket P
$\mathcal{L}_{\text{top}}(P)$	Top-K shortlist of ligands for pocket P by base GLYBATOMAQ score
$\mathcal{L}_{\text{top}}^{\text{cons}}$	Consensus shortlist pooled across pockets
$\mathcal{P}(T)$	Set of pockets considered for target T
$D(P, L)$	Docking oracle score (lower is better, by the defined convention)
$S_B(P, L)$	Base GLYBATOMAQ score prior to quantum enrichment
$S_{\text{DFT}}(P, L)$	DFT-proxy branch refinement score
$S_{\text{QMC}}(P, L)$	QMC-style proxy branch refinement score (uncertainty-aware)
$S_{\text{MQW}}(P, L)$	MQWalk topology-consistency audit / propagation score
$S_{\text{final}}^{(+)}(P, L)$	Final fused quantum-enriched GLYBATOMAQ™ score
$S_{\text{cons}}^{(+)}(L)$	Consensus score across pockets after quantum enrichment
$S_{\text{cons}}(L)$	Consensus score before quantum enrichment

ρ_P, ρ_L	PSD operator representations of pocket and ligand features
$K(P,L)$	Unnormalized trace-overlap kernel, K=Tr(ρ_P ρ_L)
$\tilde{K}(P,L)$	Normalized trace-overlap kernel
ε	Small positive numerical stabilizer
N_A	Avogadro constant used here as deterministic magnitude conditioner
$s(\alpha)$	Avogadro-conditioning factor, s(α)=exp(-αlog N_A)
α	Avogadro-conditioning exponent / scaling hyperparameter
$f_k, z_k, \tilde{f}_k, \hat{f}_k$	Raw, robust-normalized, Avogadro-conditioned, and bounded feature channel values
MAD	Median absolute deviation
Conf(L)	Conformer ensemble of ligand L
χ_c	c-th conformer of ligand L
$\chi^\star(P,L)$	Selected conformer/geometry for quantum refinement
$O(P,L)$	Unified candidate object passed to DFT-proxy/QMC-style proxy/ MQWalk branches
DFT	Density functional theory
SCF	Self-consistent field
$\psi_i(r)$	Kohn–Sham orbital
ϵ_i	Kohn–Sham orbital energy eigenvalue
$V_{\text{eff}}(r)$, $V_{xc}(r)$	Effective and exchange-correlation Kohn–Sham potentials
$E[\rho]$	DFT energy functional
E_{DFT}	DFT total electronic energy (branch descriptor)
Δ_{HL}	Frontier-orbital gap proxy (e.g., HOMO–LUMO gap)
μ	Dipole-related summary (if included)
q_{stats}	Charge distribution summary statistics
SCFdiag	SCF convergence diagnostics summary
$\Phi_{\text{DFT}}(P,L)$	DFT descriptor vector
β_{DFT}	Coefficient vector for linear DFT-proxy branch score
QMC	Quantum Monte Carlo (VMC/ DMC-style)
VMC / DMC	Variational / Diffusion Monte Carlo
Ψ, Ψ_0	Trial wave function; initial trial wave function
$\hat{H}$	Hamiltonian operator
$\hat{E}_{\text{QMC}}(P,L)$	Estimated QMC energy-like quantity
σ_{QMC}	QMC-style proxy uncertainty summary (SD/SE)
CIwidth	Confidence interval width for QMC estimate
ESS	Effective sample size
$\Phi_{\text{QMC}}(P,L)$	QMC descriptor vector
$\lambda_\sigma, \lambda_c$	Penalty weights for QMC-style proxy uncertainty terms
r_DFT(P,L)	DFT-proxy branch reliability factor in [0,1]
r_QMC(P,L)	QMC-style proxy branch reliability factor in [0,1]
MQWalk	Avogadro-conditioned topology walk/teleport validation module
W	Bipartite adjacency matrix built from $\tilde{K}$
D (graph)	Degree matrix associated with W (distinct from docking score D(P,L))
A	Degree-normalized adjacency matrix, $A = D^{-1/2} W D^{-1/2}$
A_γ	Teleportation-mixed normalized adjacency matrix
γ	Teleportation mixing coefficient
$\tilde{L}$	Avogadro-conditioned graph Laplacian
U(t)	MQWalk propagation operator, $U(t) = \exp(-it\tilde{L})$
t	Walk time / propagation hyperparameter
S_MQW(P,L)	Ligand-side propagation score from MQWalk
Δ_topo(P,L)	Topology disagreement penalty
λ_walk, λ_disc	MQWalk mixing and topology-disagreement weights
$R_0(P,L)$, $R^+(P,L)$	Pre- and post-refinement ranks
ΔR(P,L)	Rank shift $R_0 - R^+$ (positive = promotion)
Π_diag(P,L)	Diagnostic penalty term in final fusion
w_0, w_DFT, w_QMC, w_MQW	Fusion weights in final score
Θ	Set of fitted/learnable refinement/fusion parameters
$\mathcal{P}(P)$	Docking-induced preference-pair set within pocket P
m	Margin parameter in pairwise ranking loss
w_ij	Pairwise ranking weight (e.g., hardness-based)
$\mathcal{A}(\Theta;P)$	Pocket-specific training/fit loss for refinement layer
$\hat{D}(P,L)$	Optional calibrated projection to docking-like reporting scale
Overlap@k(P)	Top-k overlap between pre/post rankings for pocket P
GLYBATOMAQ_HMC	GLYBATOMAQ Hyper Mega Core conceptual modular scaffold

*R*1,*R*2	Mapped HMC attachment handles for sulfonate-cap and piperazine-tail substitution
X1–X5	HMC motif-emphasis computational variant families
Markush/YAML	Enumeration schema describing mapped core, reactions, and fragment catalogs
Hierarchical consensus hypercore	Family-level scaffold architecture + shared pharmacophore grammar representation (not literal atom-level fused scaffold)

References

1. Trott O, Olson AJ (2010) AutoDock Vina: improving the speed and accuracy of docking with a new scoring function, efficient optimization, and multithreading. J Comput Chem 31: 455-461.
2. Morris GM, Huey R, Lindstrom W, Sanner MF, Belew RK, et al. (2009) AutoDock4 and AutoDockTools4: automated docking with selective receptor flexibility. J Comput Chem 30: 2785-2791.
3. Friesner RA, Banks JL, Murphy RB, Halgren TA, Klicic JJ, et al. (2004) Glide: a new approach for rapid, accurate docking and scoring. 1. Method and assessment of docking accuracy. J Med Chem 47: 1739-1749.
4. Kitchen DB, Decornez H, Furr JR, Bajorath J (2004) Docking and scoring in virtual screening for drug discovery: methods and applications. Nat Rev Drug Discov 3: 935-949.
5. Warren GL, Andrews CW, Capelli AM, Clarke B, LaLonde J, et al. (2006) A critical assessment of docking programs and scoring functions. J Med Chem 49: 5912-5931.
6. Pagadala NS, Syed K, Tuszynski J (2017) Software for molecular docking: a review. Biophys Rev 9: 91-102.
7. Guedes IA, Pereira FSS, Dardenne LE (2018) Empirical scoring functions for structure-based virtual screening: applications, critical aspects, and challenges. Front Pharmacol 9: 1082.
8. Guedes IA, Pereira da Silva MM, Galheigo M, Krempser E, de Magalhães CS, et al. (2024) DockThor-VS: a free platform for receptor-ligand virtual screening. J Mol Biol 436: 168548.
9. Wang R, Fang X, Lu Y, Yang CY, Wang S (2005) The PDBbind database: methodologies and updates. J Med Chem 48: 4111-4119.
10. Huang N, Shoichet BK, Irwin JJ (2006) Benchmarking sets for molecular docking. J Med Chem 49: 6789-6801.
11. Mysinger MM, Carchia M, Irwin JJ, Shoichet BK (2012) Directory of Useful Decoys, Enhanced (DUD-E): better ligands and decoys for better benchmarking. J Med Chem 55: 6582-6594.
12. Schölkopf B, Smola AJ (2002) Learning with kernels: support vector machines, regularization, optimization, and beyond. Cambridge (MA): MIT Press.
13. Cortes C, Vapnik V (1995) Support-vector networks. Mach Learn 20: 273-297.
14. Rasmussen CE, Williams CKI (2006) Gaussian processes for machine learning. Cambridge (MA): MIT Press.
15. Bhatia R (2007) Positive definite matrices. Princeton (NJ): Princeton University Press.
16. Mason JC, Handscomb DC (2003) Chebyshev polynomials. Boca Raton (FL): CRC Press.
17. Trefethen LN (2013) Approximation theory and approximation practice. Philadelphia (PA): SIAM.
18. Abramowitz M, Stegun IA, (1965) Editors. Handbook of mathematical functions with formulas, graphs, and mathematical tables. New York: Dover.
19. Olver FWJ, Lozier DW, Boisvert RF, Clark CW (2010) Editors. NIST handbook of mathematical functions. Cambridge: Cambridge University Press.
20. Andrews GE, Askey R, Roy R (1999) Special functions. Cambridge: Cambridge University Press.
21. Koekoek R, Lesky PA, Swarttouw RF (2010) Hypergeometric orthogonal polynomials and their q-analogues. Berlin: Springer.
22. Berman HM, Westbrook J, Feng Z, Gilliland TN, Bhat H, et al. (2000) The Protein Data Bank. Nucleic Acids Res 28: 235-242.
23. Asojo OA, Koski RA, Bonafé N (2011) Structural studies of human glioma pathogenesis-related protein 1. Acta Crystallogr D Biol Crystallogr 67: 847-855.
24. (2026) RCSB Protein Data Bank. PDB ID 3Q2U: Structure of human glioma pathogenesis-related protein 1 [Internet]. Accessed.
25. (2026) RCSB Protein Data Bank. PDB ID 3Q2R: Crystal structure of sGLIPR1 soaked with zinc chloride [Internet]. Accesse.
26. Le Guilloux V, Schmidtke P, Tuffery P (2009) Fpocket: An open source platform for ligand pocket detection. BMC Bioinformatics 10: 168.
27. Landrum G (2006) RDKit: Open-source cheminformatics [Internet].
28. Morgan HL (1965) The generation of a unique machine description for chemical structures-A technique developed at Chemical Abstracts Service. J Chem Doc 5: 107-113.
29. Rogers D, Hahn M (2010) Extended-connectivity fingerprints. J Chem Inf Model 50: 742-754.
30. Weininger D, SMILES (1988) A chemical language and information system. 1. Introduction to methodology and encoding rules. J Chem Inf Comput Sci 28: 31-36.
31. Krenn M, Häse F, Nigam A, Friederich P, Aspuru-Guzik A (2020) Self-referencing embedded strings (SELFIES): a 100% robust molecular string representation. Mach Learn Sci Technol 1: 045024.
32. Kusner MJ, Paige B, Hernández-Lobato JM (2017) Grammar variational autoencoder. In: Proc ICML p1945-1954.
33. Jin W, Barzilay R, Jaakkola T (2018) Junction tree variational autoencoder for molecular graph generation. In: Proc ICML p2323-2332.
34. You J, Liu B, Ying Z, Pande V, Leskovec J (2018) Graph convolutional policy network for goal-directed molecular graph generation. In: Adv Neural Inf Process Syst p6410-6421.
35. Segler MHS, Kogej T, Tyrchan C, Waller MP (2018) Generating focused molecule libraries for drug discovery with recurrent neural networks. ACS Cent Sci 4: 120-131.
36. Gómez-Bombarelli R, Wei JN, Duvenaud D, Hernández-Lobato JM, Sánchez-Lengeling B, et al. Automatic chemical design using a data-driven continuous representation of molecules. ACS Cent Sci 4: 268-276.
37. Gilmer J, Schoenholz SS, Riley PF, Vinyals O, Dahl GE (2017) Neural message passing for quantum chemistry. In: Proc ICML p1263-1272.
38. Kipf TN, Welling M (2017) Semi-supervised classification with graph convolutional networks. In: Proc ICLR.
39. Vaswani A, Shazeer N, Parmar N, Uszkoreit J, Jones L, et al. (2017) Attention is all you need. In: Adv Neural Inf Process Syst p5998-6008.
40. Mohr PJ, Newell DB, Taylor BN (2021) CODATA

recommended values of the fundamental physical constants: 2018. Rev Mod Phys 93: 025010.
41. Hohenberg P, Kohn W (1964) Inhomogeneous electron gas. Phys Rev 136: B864-B871.
42. Kohn W, Sham LJ (1965) Self-consistent equations including exchange and correlation effects. Phys Rev 140: A1133-A1138.
43. Parr RG, Yang W (1989) Density-functional theory of atoms and molecules. New York: Oxford University Press.
44. Martin RM, Reining L, Ceperley DM (2016) Interacting electrons: theory and computational approaches. Cambridge: Cambridge University Press.
45. Foulkes WMC, Mitas L, Needs RJ, Rajagopal G (2001) Quantum Monte Carlo simulations of solids. Rev Mod Phys 73: 33-83.
46. Needs RJ, Towler MD, Drummond ND, López Ríos P (2010) Continuum variational and diffusion quantum Monte Carlo calculations. J Phys Condens Matter 22: 023201.
47. Nielsen MA, Chuang IL (2010) Quantum computation and quantum information. 10th anniversary ed. Cambridge: Cambridge University Press.
48. Arndt M, Juffmann T, Vedral V (2009) Quantum physics meets biology. HFSP J 3: 386-400.
49. Nunn AVW, Guy GW, Bell JD (2022) Thermodynamics and inflammation: insights into quantum biology and ageing. Quantum Rep 4: 47-74.
50. Li J, Zhu X, Zhang W, Wang J (2024) A ranking-based problem transformation method for weakly supervised multi-label learning. Pattern Recognit 153: 110505.
51. Liu Z, Huang S, Jin W, Mu Y (2024) Local kernels based graph learning for multiple kernel clustering. Pattern Recognit 150: 110300.
52. Ju W, Mao Z, Qiao Z, Qin Y, Ren P, et al. (2024) Focus on informative graphs! Semi-supervised active learning for graph-level classification. Pattern Recognit 153: 110567.
53. Yao HY, Zhang CY, Yao ZL, Chen CLP, Hu J (2024) A recurrent graph neural network for inductive representation learning on dynamic graphs. Pattern Recognit 154: 110577.
54. Chen W, Yan W, Wang W (2024) Adaptive propagation deep graph neural networks. Pattern Recognit 154: 110607.
55. Chen X, Li S, Liu R, Shi B, Xu K (2025) Molecular graph contrastive learning with line graph. Pattern Recognit 162: 111380.
56. Provost JP, Vallee G (1980) Riemannian structure on manifolds of quantum states. Commun Math Phys 76: 289-301.
57. Berry MV (1984) Quantal phase factors accompanying adiabatic changes. Proc R Soc Lond A 392: 45-57.
58. Braunstein SL, Caves CM (1994) Statistical distance and the geometry of quantum states. Phys Rev Lett 72: 3439-3443.
59. Bures D (1969) An extension of Kakutani's theorem on infinite product measures to the tensor product of semifinite w*-algebras. Trans Am Math Soc 135: 199-212.
60. Uhlmann A (1976) The transition probability in the state space of a *-algebra. Rep Math Phys 9: 273-279.
61. Bengtsson I, Zyczkowski K (2006) Geometry of Quantum States: An Introduction to Quantum Entanglement. Cambridge: Cambridge University Press.
62. Petz D (1996) Monotone metrics on matrix spaces. Linear Algebra Appl 244: 81-96.
63. Amari S (2016) Information Geometry and Its Applications. Tokyo: Springer.
64. Kempe J (2003) Quantum random walks: an introductory overview. Contemp Phys 44: 307-327.
65. Halgren TA (1996) Merck molecular force field. I. Basis, form, scope, parameterization, and performance of MMFF94. J Comput Chem 17: 490-519.
66. De Cao N, Kipf T (2018) MolGAN: An implicit generative model for small molecular graphs arXiv:1805.11973.
67. Shi C, Luo S, Xu M, Tang J (2020) GraphAF: a flow-based autoregressive model for molecular graph generation. In: Proc ICLR.
68. Jumper J, Evans R, Pritzel A, Green T, Figurnov M, et al. (2021) Highly accurate protein structure prediction with AlphaFold. Nature 596: 583-589.
69. Abramson J, Adler J, Dunger J, Evans R, Green T, et al. Accurate structure prediction of biomolecular interactions with AlphaFold 3. Nature 630: 493-500.
70. Corso G, Stärk H, Jing B, Barzilay R, Jaakkola T (2023) DiffDock: diffusion steps, twists, and turns for molecular docking. In: Proc ICLR.